Chapter 2

Large and unexpected enrichment in stratospheric $^{16}O^{13}C^{18}O$

Adapted from Yeung, L. Y., H. P. Affek, K. J. Hoag, W. Guo, A. A. Wiegel, E. L. Atlas, S. M. Schauffler, M. Okumura, K. A. Boering, and J. M. Eiler (2009), Large and unexpected enrichment in stratospheric $^{16}O^{13}C^{18}O$ and its meridional variation, *Proc. Natl. Acad. Sci. U. S. A.*, *106*(28), 11,496–11,501.

2.1 Abstract

The stratospheric CO_2 oxygen isotope budget is thought to be governed primarily by the $O(^1D)$ + CO_2 isotope exchange reaction. However, there is increasing evidence that other important physical processes may be occurring that standard isotopic tools have been unable to identify. Measuring the distribution of the exceedingly rare CO_2 isotopologue $^{16}O^{13}C^{18}O$, in concert with ^{18}O and ^{17}O abundances, provides sensitivities to these additional processes, and thus is a valuable test of current models. We identify a large and unexpected meridional variation in stratospheric $^{16}O^{13}C^{18}O$, observed as proportions in the polar vortex that are higher than in any naturally derived CO_2 sample to date. We show, through photochemical experiments, that lower $^{16}O^{13}C^{18}O$ proportions observed in the mid-latitudes are determined primarily by the $O(^1D)$ + CO_2 isotope exchange reaction, which promotes a stochastic isotopologue distribution. In contrast, higher $^{16}O^{13}C^{18}O$ proportions in the polar vortex show correlations with long-lived stratospheric tracer and bulk isotope abundances opposite to those observed at mid-latitudes, and thus opposite to those easily explained by $O(^1D)$ + CO_2. We believe the most plausible explanation for this meridional variation is either an unrecognized isotopic fractionation associated with the mesospheric photochemistry of CO_2 or a temperature-dependent isotopic exchange on polar stratospheric clouds (PSCs). Unraveling the ultimate source of stratospheric $^{16}O^{13}C^{18}O$ enrichments may impose additional isotopic constraints on biosphere-atmosphere carbon exchange, biosphere productivity, and their respective responses to climate change.

2.2 Introduction

Predicting future CO_2 concentrations and carbon cycle-climate feedbacks depends on one's ability to quantify the contributions from the sources and sinks governing the global carbon budget and how they may change over time. The bulk stable isotope composition of CO_2 (i.e., its $^{13}C/^{12}C$, $^{18}O/^{16}O$, and $^{17}O/^{16}O$ ratios) plays an important role in constraining this budget (see *Yakir* [2003] and references therein). In the stratosphere, the oxygen-isotope composition of CO_2 is thought to be modified by oxygen isotope exchange reactions with $O(^1D)$ generated by ozone photolysis [*Yung et al.*, 1997], whereas in the troposphere it is controlled by isotope exchange reactions with liquid water in the oceans, soils, and plant leaves [*Ciais and Meijer*, 1998]. The interplay between stratospheric and tropospheric isotope exchange reactions, in principle, could allow the relative abundances of $^{12}C^{16}O_2$, $^{16}O^{12}C^{18}O$, and $^{16}O^{12}C^{17}O$ isotopologues to be used as tracers for gross biosphere productivity [*Hoag et al.*, 2005; *Luz et al.*, 1999], but the stratospheric CO_2 photochemical system is still under-constrained and our understanding of it is incomplete.

Discrepancies between laboratory and stratospheric measurements [*Lämmerzahl et al.*, 2002; *Shaheen et al.*, 2007; *Thiemens et al.*, 1995] have prompted questions about whether the $O(^1D)$ + CO_2 isotope exchange reaction acts alone on stratospheric CO_2 or whether other photochemical [*Bhattacharya et al.*, 2000] or dynamical [*Boering et al.*, 2004] processes significantly affect the stable isotopologue distribution in CO_2. Stratospheric oxygen isotope covariations in CO_2 [*Kawagucci et al.*, 2008; *Lämmerzahl et al.*, 2002; *Liang et al.*, 2008] consistently differ from those found in laboratory experiments simulating stratospheric photochemistry [*Baulch and Breckenridge*, 1966; *Chakraborty and Bhattacharya*, 2003; *Johnston et al.*, 2000; *Shaheen et al.*, 2007; *Wen and Thiemens*, 1993], and the origin of this disagreement is still uncertain because bulk stable isotope measurements alone (i.e., of $\delta^{13}C$, $\delta^{18}O$, and $\delta^{17}O$ values) cannot differentiate extrinsic effects [e.g., the $O(^1D)$ isotope composition] from intrinsic (i.e., photolytic or kinetic isotope) effects on the isotope composition of stratospheric CO_2. Additional constraints arising from analysis of multiply-substituted isotopologues of CO_2 can provide sensitivities to these processes [*Affek and Eiler*, 2006; *Affek et al.*, 2007; *Eiler*, 2007; *Eiler and Schauble*, 2004]. To investigate stratospheric

CO_2 chemistry, we examine here the proportions of $^{16}O^{13}C^{18}O$ (reported as a Δ_{47} value) in stratospheric CO_2 and in laboratory kinetics experiments.

2.3 Field sample collection and analysis

Twelve stratospheric CO_2 samples were analyzed for bulk stable isotope compositions and Δ_{47} values: Six samples of stratospheric CO_2 were collected from the NASA ER-2 aircraft during the 1999/2000 Arctic winter Stratospheric Aerosol and Gas Experiment III (SAGE III) Ozone Loss and Validation Experiment (SOLVE) campaign [*Newman et al.*, 2002], and six samples were collected from a balloon flight from Fort Sumner, New Mexico on 29 September 2004. SOLVE mission samples (January – March 2000, 29 – 79°N, 11 – 20 km) were collected as whole air samples [*Flocke et al.*, 1999]. CO_2 was then isolated from the ~5 L STP of air by a combination of liquid N_2 and ethanol-dry ice traps, then separated into aliquots of 12 – 18 μmol CO_2 each and sealed into glass ampoules. Balloon samples were collected using a cryogenic whole air sampler (34.5°N, 103.6°W, 27 – 33 km) [*Froidevaux et al.*, 2006; *Lueb et al.*, 1975] and purified and stored as above.

$\delta^{13}C$, $\delta^{18}O$, and $\delta^{17}O$ of CO_2 were measured on a Finnigan MAT 252 isotope ratio mass spectrometer (IRMS) at UC-Berkeley. $\Delta^{17}O$ was measured using the CeO_2 technique with a precision of ± 0.5‰ [*Assonov and Brenninkmeijer*, 2001]. Aliquots of the same CO_2 samples were analyzed for Δ_{47} using a Finnigan MAT 253 IRMS at Caltech configured to collect masses 44 – 49, inclusive, and standardized by comparison with CO_2 gases of known bulk isotopic composition that had been heated for two hours at 1000°C to achieve a stochastic isotopic distribution [*Eiler and Schauble*, 2004]. Masses 48 and 49 were used to detect residual hydrocarbon contamination. For Δ_{47} analysis, the 12 – 18 μmol aliquots of SOLVE-mission and balloon CO_2 samples were purified of potential contaminants, such as hydrocarbons, by a pentane-liquid N_2 slush (–120°C) as well as by passing it through a gas chromatographic (GC) column (Supleco Qplot, 530 μm ID, 30 m length) at –20°C, with column baking at 150°C between samples [*Affek and Eiler*, 2006; *Ghosh et al.*, 2006]. All data were corrected for the presence of N_2O using the method described previously [*Affek and Eiler*, 2006]. Each measurement consisted of 5 – 9 acquisitions (of 10 measurement

Table 2.1: Stratospheric air sample data

Air Type*	Sample Name	Altitude (km)	Latitude (°N)	θ (K)	CH_4 (ppbv)	N_2O (ppbv)	CFC-11 (pptv)	CFC-12 (pptv)	$\delta^{13}C$ (‰)	$\delta^{18}O$ (‰)	$\Delta^{17}O$ (‰)	Δ_{47} (‰)
ER-2 samples												
V	20000312(25)1120	19.33	79.2	443.61	948	111.5	19.	147.	-8.11	44.55	5.76	1.614
V	20000131(30)1001	19.85	73.5	448.08	1066	142.1	31.	198.	-8.08	43.62	4.38	1.555
V	20000203(10)1173	17.63	70.4	409.37	1250	192.8	72.	293.	-8.06	43.06	3.69	1.436
VE	20000127(5)1060	19.45	57.7	445.10	1385	227.6	112.	362.	-8.07	42.79	2.45	1.233
M	20000106(30)1169	19.40	29.3	467.43	1495	256.4	157.	421.	-8.08	42.50	2.13	1.071
M	20000111(25)2021	11.40	43.5	358.26	1726	307.9	246.	526.	-8.06	40.98	0.18	1.075
Balloon samples												
M	1-A010-R (2035)	33.34	34.5	931.14	835	54.0	0.13	46.0	-8.07	45.14	6.46	0.976
M	3-A01-R (1141)	32.22	34.6	896.15	843	56.7	0.23	51.2	-7.99	45.44	6.29	0.923
M	5-A013-R (2079)	30.78	34.6	861.84	913	77.8	0.15	78.2	-8.03	45.14	5.91	0.913
M	7-A026-R (1057)	29.26	34.6	778.08	957	92.1	0.63	100.2	-8.07	44.98	6.12	0.912
M	8-A017-E (1113)	28.73	34.6	757.89	1014	107.9	1.10	78.2	-8.04	44.79	5.00	1.004
M	10-A022-E (1186)	27.27	34.6	709.67	1176	155.9	5.90	123.6	-8.03	44.09	4.26	0.916

*Air type is abbreviated as V = vortex, VE = vortex edge, and M = mid-latitude based on N_2O:θ correlations, where θ is potential temperature in Kelvin. Non-isotopic tracer measurement methodology can be found in *Flocke et al.* [1999] and *Froidevaux et al.* [2006].

cycles each), with typical standard deviations (acquisition-to-acquisition) of 0.06‰ in Δ_{47}.

2.4 Field results

The stratospheric samples (see Table 2.1) display Δ_{47} values both higher and more variable than those exhibited by tropospheric air at the surface, which has an average Δ_{47} value of 0.92 ± 0.01‰ in remote regions (Cape Grim, Tasmania and Barrow, Alaska) [*Affek et al.*, 2007]. The high-latitude (> 57°N) stratospheric samples, in particular, are significantly more enriched in Δ_{47} than any material analyzed before in nature (see Figure 2.1 and see *Affek et al.* [2007] and *Eiler* [2007]). At high latitudes, Δ_{47} varies strongly and increases monotonically with decreasing mixing ratios of long-lived trace gases that have tropospheric sources and stratospheric sinks, such as N_2O and CH_4. At mid-latitudes, Δ_{47} varies relatively little and shows correlations with trace gas mixing ratios having the opposite sign of those observed at high latitudes (see Figure 2.2 and Table 2.1). Using the correlation between simultaneously measured N_2O mixing ratios and potential temperature [*Greenblatt et al.*, 2002], we found that the high-latitude samples were collected in inner polar vortex air (three samples) or vortex edge air (one sample). Thus, differences in the sign and magnitude of Δ_{47} variations with N_2O mixing ratio in the two subsets of

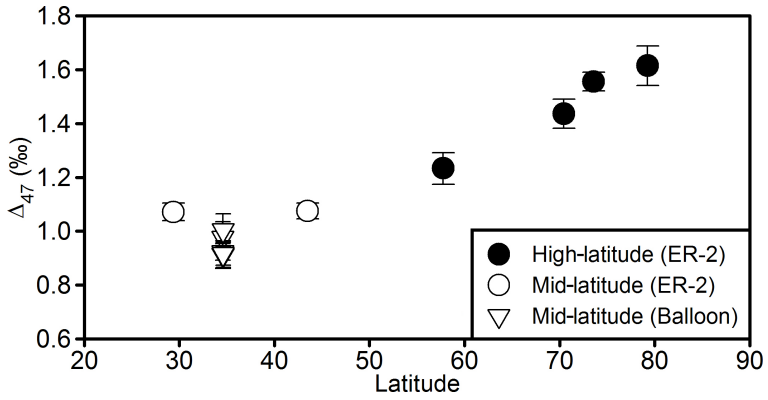

Figure 2.1: **Meridional variation of Δ_{47} measured in stratospheric samples.** Typical values in the troposphere are $\Delta_{47} \sim 0.9$‰. Error bars show 2σ standard errors.

samples are presumably due to differences between vortex and non-vortex processes. In contrast to these Δ_{47} trends, covariations of $\Delta^{17}O$ with $\delta^{18}O$ and mixing ratios of long-lived trace gases for our mid-latitude samples resemble those of our polar vortex samples (or show the expected differences for slightly shorter-lived tracers, e.g., CFC-11) and also those reported in earlier studies of high-latitude [*Boering et al.*, 2004; *Kawagucci et al.*, 2008] and polar vortex air (see Figure 2.3) [*Alexander et al.*, 2001]. This suggests that Δ_{47} records a process to which $\Delta^{17}O$ is not sensitive.

In order to rule out the possibility that the observed high Δ_{47} values result from sample contamination by organic compounds in the stratospheric samples, one of the samples [20000131(30)1001] was exposed to water at 25°C for 24 hours to reach CO_2–water isotopic equilibrium. The exchanged sample had a Δ_{47} value of 0.862 ± 0.078‰, identical to the cylinder CO_2 working standard, whose Δ_{47} value reflects CO_2 isotopic equilibrium at room temperature [*Wang et al.*, 2004]. In contrast, the presence of contaminants would have resulted in a high Δ_{47} value even after isotopic equilibrium was reached. Hence, no evidence for contamination was observed in the high-latitude samples.

2.5 Laboratory photochemical experiments

To gain further insight into the correlations we observed between Δ_{47}, $\Delta^{17}O$, and $\delta^{18}O$, we conducted several laboratory photochemistry experiments. Enrichments of $\Delta^{17}O$ and $\delta^{18}O$

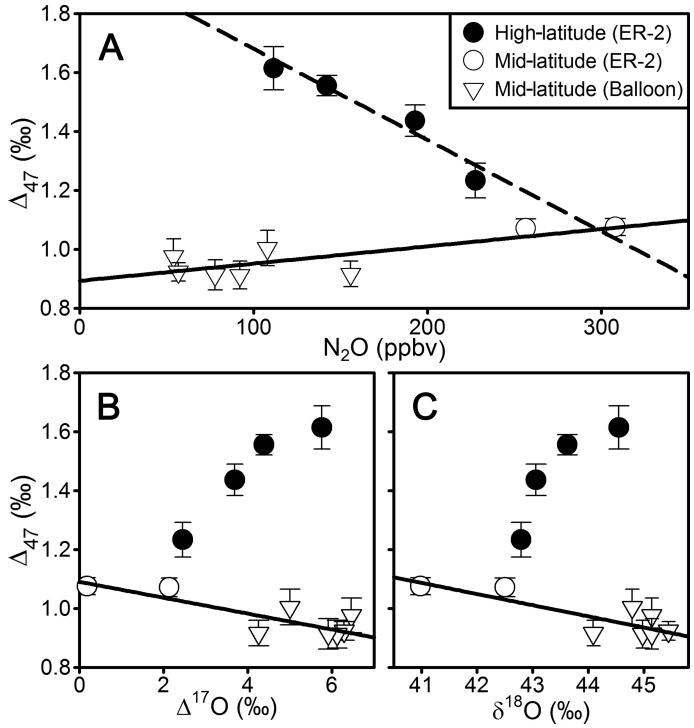

Figure 2.2: **Correlation between Δ_{47} and stratospheric tracers.** (**A**), best-fit lines are shown for mid-latitude (solid line) and high-latitude (dashed line) Δ_{47} vs. N_2O mixing ratio. Correlations between Δ_{47} and other tracers with tropospheric sources and stratospheric sinks are similar (see Figure 2.3). Also shown is the best-fit line of (**B**), Δ_{47} vs. $\Delta^{17}O$, and (**C**), Δ_{47} vs. $\delta^{18}O$ in mid-latitude air, which is used to estimate the integrated effective isotopic composition of stratospheric $O(^1D)$ (see text). Error bars represent 2σ standard errors.

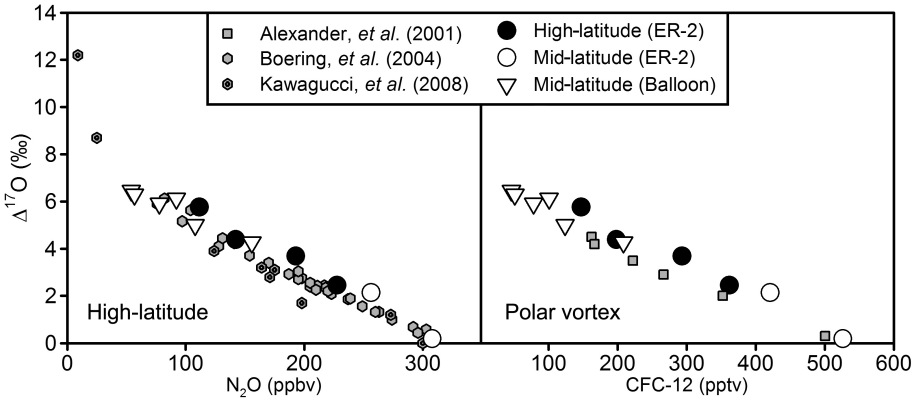

Figure 2.3: **$\Delta^{17}O$ values vs. long-lived stratospheric tracer mixing ratios.** In both panels, measurements reported in this work (ER-2 and Balloon data) are compared with previous high-latitude ($> 48^\circ$N; left panel) and polar vortex (right panel) measurements. The measured $\Delta^{17}O$ correlations with N_2O and CFC-12 do not reveal obvious distinctions among the mid- and high-latitude CO_2 samples; Δ_{47} measurements, in contrast, reveal strong mesospheric or other polar vortex influence.

in stratospheric CO_2 are generally understood to arise from isotope exchange with $O(^1D)$, which is produced by photolysis of ^{18}O- and ^{17}O-enriched stratospheric ozone [*Liang et al.*, 2007; *Yung et al.*, 1997], but the kinetics of the isotope exchange reactions for multiply-substituted isotopologues of CO_2, and their effects on Δ_{47}, have not yet been explored. Changes in Δ_{47} caused by these reactions should principally reflect relative changes in $^{16}O^{13}C^{18}O$ and $^{16}O^{12}C^{18}O$ abundances because the ^{13}C composition is not affected by isotope exchange with $O(^1D)$; variations in $^{17}O^{12}C^{18}O$ and $^{13}C^{17}O_2$ abundances will change Δ_{47} more subtly. Thus, reactions 2.1 and 2.2 are most relevant.

$$^{18}O(^1D) + {}^{12}C^{16}O_2 \rightarrow {}^{18}O^{12}C^{16}O_2^* \rightarrow {}^{16}O + {}^{16}O^{12}C^{18}O \quad (2.1)$$

$$^{18}O(^1D) + {}^{13}C^{16}O_2 \rightarrow {}^{18}O^{13}C^{16}O_2^* \rightarrow {}^{16}O + {}^{16}O^{13}C^{18}O \quad (2.2)$$

Statistical partitioning of isotope exchange products, through a process governed by random chance such that $^{18}O(^1D)$ has a 2/3 probability of being incorporated into the product CO_2, would drive the CO_2 isotopologues towards a stochastic distribution (i.e., $\Delta_{47} = 0$). If any one (or more) of the isotope exchange reactions does not partition products statistically, however, Δ_{47} can increase [e.g., if $^{18}O(^1D)$ exchanges isotopes with $^{13}C^{16}O_2$ more readily than with $^{12}C^{16}O_2$] or decrease accordingly.

Two sets of laboratory experiments were conducted. First, the relative rates of reactions 2.1 and 2.2 were probed directly to obtain the $^{13}C/^{12}C$ kinetic isotope effect (KIE) for the $^{18}O(^1D)$ + CO_2 isotope exchange reaction at 300 K and 229 K. These experiments used pulsed photolysis of 97% $N_2{}^{18}O$ at 193 nm as a source of $^{18}O(^1D)$, and the extent of isotope exchange was minimized. Second, we performed continuous-irradiation experiments, using a mercury lamp, on mixtures of isotopically unlabeled O_2, O_3, and CO_2 as a function of different irradiation times to determine the aggregate effects of the $O_2/O_3/CO_2$ photochemical system on Δ_{47}.

2.5.1 $^{13}C/^{12}C$ kinetic isotope effect experiments

2.5.1.1 Methods overview

For experiments performed at 300 K, a 15 cm-long stainless steel conflat chamber with quartz windows was used as a reaction chamber. Low-temperature experiments were performed in a 25 cm-long, all-quartz chamber, cooled to 229 K under vacuum via direct conduction with a cold copper jacket (see Appendix 2.C). Experiments were initiated with pulsed excimer laser photolysis of $N_2{}^{18}O$ (193 nm, 50 – 100 mJ pulse^{-1}, 1 Hz repetition rate, $<$ 200 pulses), producing $^{18}O(^1D)$, in $\sim$1:100:3000 static mixtures of $N_2{}^{18}O$:CO_2:He (100 Torr total pressure). $N_2{}^{18}O$ was synthesized from the acid-catalyzed reduction of ^{18}O-labeled aqueous $NaNO_2$ [*McIlvin and Altabet*, 2005; *Samuel and Wassermann*, 1971]; a detailed description of its synthesis and characterization can be found in Section 2.5.1.2. A schematic of the reaction scheme is shown in Figure 2.4.

Starting samples of CO_2 contained a stochastic distribution of isotopologues, generated in the manner described in Section 2.3. The initial CO_2 isotopic composition was measured and CO_2 was recollected cryogenically for use in the reaction chamber. Residence time in the reaction chamber had a negligible effect on Δ_{47} in the 300 K experiments, whereas the chamber cooling process alone was observed to enrich the starting material in $\delta^{18}O$ and Δ_{47}, by 0.5‰ and 0.13‰, respectively. These offset values were subtracted from final $\delta^{18}O$

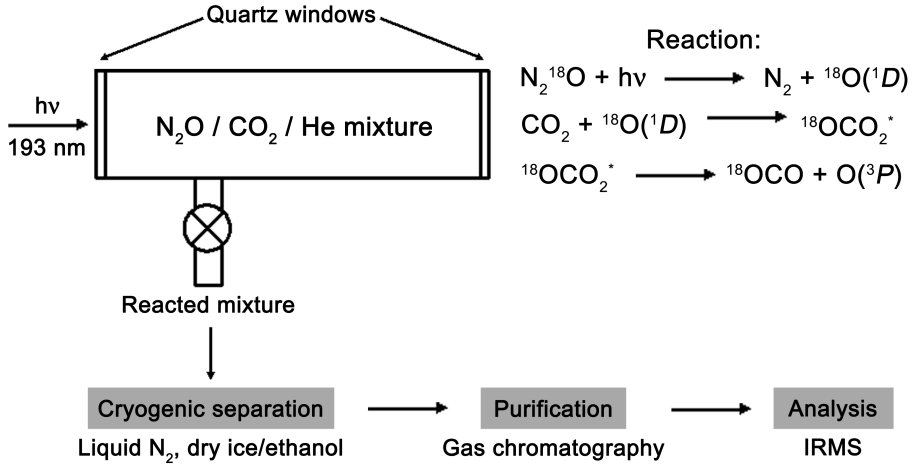

Figure 2.4: **Schematic of O(^1D) + CO_2 reaction-purification-analysis procedure.**

and Δ_{47} values in 229 K experiments. The reaction products were recollected cryogenically and purified in two GC steps. Separation of residual $N_2{}^{18}O$ and reacted CO_2 was achieved through a packed-column (PoraPak Q) GC separation at 25°C, after which the samples were purified with a capillary GC as described above. Due to the presence of $N_2{}^{18}O$ isobars with CO_2 at masses 46 – 49, mass 14 was also monitored to measure the extent of $N_2{}^{18}O$ contamination. Differences in mass-14 signal between the starting and product material of greater than 5 mV (a variation typical of 'clean' laboratory standards) were deemed contaminated, and the data points were rejected.

The difference between the initial and final $\delta^{18}O$ (hereafter referred to as $\Delta\delta^{18}O$) and Δ_{47} compositions was calculated assuming that $\delta^{13}C$ was unchanged, since there was no external carbon reservoir in the reaction. GC separation of $N_2{}^{18}O$ and CO_2 yielded a small, yet reproducible Δ_{47} change of +0.13‰, which was present both when gases of stochastic isotope composition were analyzed as well as when aliquots of cylinder CO_2 working standard (Δ_{47} = 0.86‰) were analyzed. The source of this offset may be a small amount of diffusive or adsorptive fractionation on the GC column, but it was not investigated further. Because of the apparent insensitivity of the Δ_{47} change to initial isotopic composition, the sample purification step was treated as a small additive effect on the measured Δ_{47}, with no effect on the overall kinetics measured.

The following sections, 2.5.1.2 and 2.5.1.3, provide a detailed description of the materials and methods utilized to obtain the results summarized in Section 2.5.1.4.

2.5.1.2 $N_2{}^{18}O$ synthesis

Precursor samples of $N_2{}^{18}O$ were synthesized from the acid-catalyzed reduction of aqueous nitrite ($NO_2{}^-$) [*McIlvin and Altabet*, 2005; *Samuel and Wassermann*, 1971]. A description of a synthesis and characterization follows. First, a solution of 0.4 mmol sodium nitrite ($NaNO_2$) in 800 μl >97% $H_2{}^{18}O$ (Isonics) was placed in a three-neck round-bottom flask and flushed with He at 30 mL min^{-1} for 20 minutes to remove any dissolved gases. The flow was then stopped and the flask closed off and put in an ice bath. 350 μl glacial acetic acid was then added through a rubber septum with a syringe to acidify the water. For 3 minutes,

the nitrite was allowed to exchange oxygen atoms fully with $H_2{}^{18}O$ in the acidic environment [*Ott*, 1981]. Then, the nitrite was reacted with 220 μl of a solution of 1.5 mmol sodium azide (NaN_3), 100 μl glacial acetic acid, and 150 μl $H_2{}^{18}O$, also added through the septum, for 40 minutes with stirring. Due to the high concentration of acid, the dominant reaction was expected to be that between nitrous acid (HNO_2) and hydrazoic acid (HN_3) to produce $N_2{}^{18}O$:

$$HNO_2 + HN_3 \rightarrow N_2O + N_2 + H_2O \tag{2.3}$$

After the 40-minute reaction time, 1 mL of a ~17 M NaOH solution was added through the septum to stop the reaction and remove any residual CO_2. The gas-phase products were collected by flowing He through the flask at 5 mL min^{-1} for 1 h into a "U-trap" held at liquid nitrogen temperature (77 K). Synthesized $N_2{}^{18}O$ was dried cryogenically using a pentane slush (–120 °C), then a dry ice/ethanol slush (–76 °C), and recollected in a trap at liquid nitrogen temperature. Chemical yield in the $N_2{}^{18}O$ was determined by expanding the product gas into a calibrated volume on a vacuum line, and the total product yield was determined to be 53% (0.195 mmol).

Table 2.2: IR band assignments for the spectra in Figure 2.5

Frequency (cm^{-1})	Band	Frequency (cm^{-1})	Band
1155	$2\nu_2$	1285	ν_1 ($^{14}N_2{}^{16}O$)
1247	ν_1	1595	ν_2 ($H_2{}^{16}O$)
1840	$\nu_1 + \nu_2{}^*$	2350	ν_3 (CO_2)
2217	ν_3	2563	$2\nu_1$ ($^{14}N_2{}^{16}O$)
2295	$4\nu_2$	3481	$\nu_1 + \nu_3$ ($^{14}N_2{}^{16}O$)
2412	$\nu_1 + 2\nu_2{}^*$	3657	ν_1 ($H_2{}^{16}O$)
2491	$2\nu_1$	3756	ν_3 ($H_2{}^{16}O$)
2787	$\nu_2 + \nu_3$		
3345	$2\nu_2 + \nu_3{}^*$		
3435	$\nu_1 + \nu_3$		
3663	$2\nu_1 + 2\nu_2{}^*$		
3737	$3\nu_1{}^*$		

Assignments taken from *Łapiński et al.*, and references therein. Literature values are ν_1 = 1247 cm^{-1}, ν_2 = 571 cm^{-1}, and ν_1 = 2217 cm^{-1} for $N_2{}^{18}O$.

*Temporary assignment because band has yet not been reported in the literature.

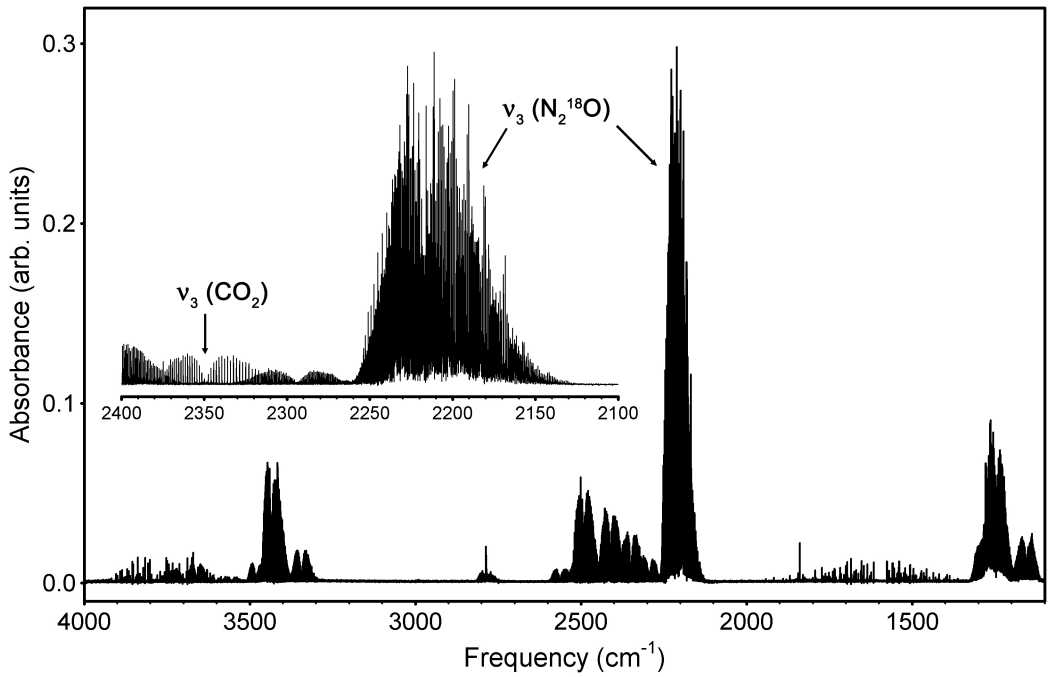

Figure 2.5: **FT-IR spectrum of synthesized $N_2{}^{18}O$ between 1100 cm^{-1} and 4000 cm^{-1}.** Inset shows the zoomed-in area between 2100–2400 cm^{-1}.

Samples were then measured on a Fourier-transform infrared spectrometer (FT-IR) for chemical purity and a IRMS for isotopic purity. FT-IR analysis was conducted on a Nicolet FT-IR spectrometer with 3 Torr $N_2{}^{18}O$, 0.125 cm^{-1} resolution, and 2000 scans in an 18 cm-pathlength cell with CaF_2 windows. Table 2.2 contains the band assignments for the $N_2{}^{18}O$ IR spectrum shown in Figure 2.5. The IR spectrum (see inset of Figure 2.5) contains a small amount of CO_2, but it is considered too small an amount to affect isotopic measurements. The absorption cross-section of the $CO_2(\nu_3)$ band is three times that of the $N_2O(\nu_3)$ band [*Rothman et al.*, 2009], yet in the experimental spectrum, the N_2O band is stronger than the CO_2 band by an order of magnitude; consequently, the concentration of CO_2 in the $N_2{}^{18}O$ sample is estimated to be 3%. Because $N_2{}^{18}O$ was used as a 1% mixture in CO_2 for the photolysis experiments, the estimated mixing ratio of contaminant CO_2 is 3×10^{-4} in the sample CO_2. This mixing ratio amounts to a maximum absolute error less than 0.001‰ in the observed $\delta^{18}O$ at natural abundance (0.2% ^{18}O), and it is therefore negligible. H_2O lines in the spectrum are believed to come from atmospheric water vapor, as they are consistent with $H_2{}^{16}O$ instead of the $H_2{}^{18}O$ used in the synthesis. Because all of the $H_2{}^{18}O$ appears

Table 2.3: IRMS ion signals from the synthesized $N_2{}^{18}O$

m/z	Signal (mV)	^{18}O content
44	1276	96.7%
46	37870	
30	482	96.8%
32	14773	

to have been removed by the cryogenic drying steps, and the sample compartment was continuously purged with dry N_2, this water vapor is believed to arise from desorbing water from the FT-IR cell walls.

Mass-spectrometric analysis was performed on a Finnigan MAT 253 using cup position 3 (3×10^{10} Ω resistor). Isotope ratios were determined at two different *m/z* ranges: 46/44 (mainly $^{14}N_2{}^{18}O/^{14}N_2{}^{16}O$) and 32/30 (mainly $^{14}N^{18}O/^{14}N^{16}O$). Table 2.3 contains the observed signals and calculated isotopic purity at 16.5 mbar in the sample bellows. Here we see that the synthesized N_2O is indeed 97% labeled with ^{18}O, and it was used in experiments without further purification.

2.5.1.3 Reaction models

Two models for the $^{13}C/^{12}C$ KIE experiments were constructed. One was a chemical kinetic model designed to calculate the expected trends in Δ_{47} vs. $\Delta\delta^{18}O$ given specific KIEs. The second was a hard-sphere collision model designed to model the velocity relaxation of the nascent $^{18}O(^1D)$, from which a collision energy distribution for each experiment could be calculated.

CHEMICAL KINETIC MODEL. A comprehensive, isotopologue-specific kinetics model of the $O(^1D)$-CO_2 photochemical experiment (144 isotope exchange reactions) was constructed in the FACSIMILE kinetics modeling package. Stochastic isotope exchange branching fractions [*Baulch and Breckenridge*, 1966; *Yung et al.*, 1997] were used: Incident $O(^1D)$ atoms had a 2/3 probability of isotope exchange, regardless of the isotope exchange reaction. The isotopic composition of the initial $O(^1D)$ was treated as a constant; for these ^{18}O-labeled

experiments, trace ^{17}O and ^{16}O abundances had negligible effects on the measured $^{13}C/^{12}C$ KIE.

We expect to observe subtle isotope effects due to differences in the $^{18}O(^1D)$–CO_2 collision frequencies between different isotopologues in the helium-buffer-gas experiments because the collision-limited rate of reaction for $O(^1D)$ + CO_2 [*Sander et al.*, 2006] implies that the reaction probability for any given $O(^1D)$–CO_2 collision is near unity. For instance, more $^{18}O(^1D)$ + $^{12}C^{16}O_2$ collisions than $^{18}O(^1D)$ + $^{13}C^{16}O_2$ collisions occur because the average velocity for $^{12}C^{16}O_2$ is higher than that for $^{13}C^{16}O_2$ at a given temperature. This reduces the rate at which reaction 2.2 occurs relative to reaction 2.1 in the laboratory by about 5%. The $O(^1D)$-CO_2 collision frequencies in these experiments scale directly with the collision pair's relative velocity, which depends inversely on the pair's reduced mass (μ) according to equation 2.4:

$$k_{2.2} = \sqrt{\frac{\mu_{^{18}O + {}^{44}CO_2}}{\mu_{^{18}O + {}^{45}CO_2}}} \times k_{2.1} = \mu_{eff} k_{2.1} \tag{2.4}$$

k represents the rate coefficient for the subscripted reaction, and μ represents the reduced mass of the subscripted reactant pair. Analogous relationships can be computed for each unique reactant pair. Δ_{47} is expected to decrease with increasing $\Delta\delta^{18}O$ because the collision frequency for $^{18}O(^1D)$ + $^{44}CO_2$ is ~5% larger than that for $^{18}O(^1D)$ + $^{45}CO_2$. Such biases are expected to be small in the atmosphere due to competing electronic quenching reactions (e.g., $O(^1D)$ + $N_2 \rightarrow O(^3P)$ + N_2) [*Johnston et al.*, 2000]. These electronic quenching reactions were minimized in our pulsed photolysis experiments because He was used as the buffer gas [*Heidner and Husain*, 1974; *Shi and Barker*, 1990]. Thus a $^{13}C/^{12}C$ KIE = $k_{2.2}/k_{2.1} = 1$ in our laboratory experiment will appear as an anti-correlation in a plot of Δ_{47} vs. $\Delta\delta^{18}O$. A $^{13}C/^{12}C$ KIE ≈ 1.01 and an $O(^1D)$ source with $\delta^{18}O = \delta^{17}O \approx 100‰$ would be required to generate the polar vortex Δ_{47} enrichment and also the polar vortex Δ_{47} vs. $\Delta^{17}O$ correlation. On the Δ_{47} vs. $\Delta\delta^{18}O$ plot, the slope would be +0.0055 using $k_{2.2}/k_{2.1} = 1.01$.

$O(^1D)$ + CO_2 COLLISION ENERGY DISTRIBUTION. The $^{13}C/^{12}C$ experiment was also modeled on the collision-by-collision level because the $O(^1D)$ + CO_2 isotope exchange reaction occurs through two reaction channels whose branching ratio depends on collision energy

[*Perri et al.*, 2003]:

$$O(^1D) + CO_2 \rightarrow O(^3P) + CO_2 \quad (2.5)$$

$$\rightarrow O(^1D) + CO_2 \quad (2.6)$$

The branching fraction of the non-quenching channel (2.6) increases significantly with reaction collision energy, E_{coll} [*Mebel et al.*, 2004; *Perri et al.*, 2004]. Observed isotope effects, then, may also depend on the distribution of E_{coll}. Nascent $O(^1D)$ atoms from the N_2O photolysis scheme employed in this study had a high average translational energy, so He was chosen as buffer gas to lower the average collision energy, $\langle E_{coll} \rangle$, to a stratospherically relevant value; He quenches the translational energy of $O(^1D)$ atoms efficiently while quenching the electronic energy inefficiently [*Heidner and Husain*, 1974; *Shi and Barker*, 1990]. Furthermore, the translational energy transfer during $O(^1D)$ + He collisions can be modeled well using a hard-sphere collision model [*Matsumi et al.*, 1994b].

We constructed a Monte Carlo hard-sphere collision model in the MATLAB programming environment based on the solution to the general elastic hard-sphere problem; the mathematical derivation can be found in the literature [*Nan and Houston*, 1992], and the program code can be found in Appendix 2.D. The basic function of the program was to calculate the final velocity vectors for two colliding hard spheres of masses m_1 (the O-atom) and m_2 (the He-atom) with initial velocity vectors (v_{1i}, θ_{1i}, ϕ_{1i}) and (v_{2i}, θ_{2i}, ϕ_{2i}), respectively.

The elastic hard-sphere calculation was performed for a distribution of initial O-atom velocities in a He bath gas at thermal equilibrium (e.g., at 298 K). First, O-atom velocity vectors, ($v_{O,i}$, $\theta_{O,i}$, $\phi_{O,i}$), were sampled according to a velocity distribution for $O(^1D)$ ejected from the photolysis of $^{14}N_2{}^{16}O$ at 193 nm [*Felder et al.*, 1991; *Hanisco and Kummel*, 1993; *Springsteen et al.*, 1993] centered at $E_T = 18.2$ kcal mol^{-1}. In the absence of experimental data for $^{14}N_2{}^{18}O$ photodissociation, the $^{18}O(^1D)$ velocity distribution was approximated by a gaussian distribution centered at $\sim$2900 m s^{-1} with a full-width at half-maximum (FWHM) of $\sim$1000 m s^{-1} (i.e., $\langle E_T \rangle \sim 18 \pm 7$ kcal mol^{-1}). Second, a He-atom velocity vector, ($v_{He,i}$, $\theta_{He,i}$, $\phi_{He,i}$), was selected randomly from a Maxwell-Boltzmann velocity distribution. Using this pair of initial conditions and a random impact parameter b (sampled with a probability proportional to itself), the final velocity vector of the O-atom after one collision, ($v_{O,f}$, $\theta_{O,f}$,

$\phi_{O,f}$), was computed and stored. The final velocity was then *re-used as an initial velocity* for the next collision with a second He-atom, whose velocity was randomly sampled as above. This calculation was repeated for up to 200 total collisions and N = 50,000 initial O(^1D) velocities, a total of 10^6 – 10^7 calculations. After 200 collisions, $>$ 96% of the O(^1D) would have reacted with CO_2 under our experimental conditions.

Using the O(^1D) velocity distribution after each O(^1D)–He collision, the distribution of O(^1D)–CO_2 collision energies, $P_j(E_{\text{coll}})$, for the jth collision could then be calculated similarly. The relative CO_2 concentration, i.e., $\rho_{CO_2} \sim 0.03$, was then used to weight the $P_j(E_{\text{coll}})$ distribution at the jth collision to obtain a O(^1D)–CO_2 collision energy distribution over the whole experiment. The results were summed according to equation 2.7:

$$P_{\text{total}}(E_{\text{coll}}) = \rho_{CO_2} \sum_j P_j(E_{\text{coll}}) \tag{2.7}$$

The model was tested by confirming that the average kinetic energy approached (and remained at) the value expected at thermal equilibrium by the equipartition theorem, e.g., $\frac{3}{2}$RT = 0.89 kcal mol^{-1} at 300 K. Calculated $P_{\text{total}}(E_{\text{coll}})$ distributions for several different experimental conditions are shown in Figure 2.6. Our simulation of the initial O(^1D) collision cascade shows that 81% of all O(^1D) + CO_2 collisions occur with $E_{\text{coll}} < 2$ kcal mol^{-1}, with $\langle E_{\text{coll}} \rangle$ = 1.6 kcal mol^{-1}, similar to the E_{coll} distribution expected in the stratosphere [*Kharchenko and Dalgarno*, 2004; *Takahashi et al.*, 2002]. As we noted earlier, the nascent ^{18}O(^1D) translational energy distribution is somewhat uncertain because the existing photodissociaton dynamics studies focused on the $^{14}N_2{}^{16}O$ molecule, not the $^{14}N_2{}^{18}O$ used in these experiments. Changing the peak of the nascent ^{18}O(^1D) translational energy distribution by 1 – 2 kcal mol^{-1} changed the average O(^1D)-CO_2 collision energy by $<$ 0.1 kcal mol^{-1}.

The shape of the laboratory $P_{\text{total}}(E_{\text{coll}})$ distribution appears different from that modeled in conditions resembling the stratosphere [*Kharchenko and Dalgarno*, 2004]; this difference is due to O(^1D) having a slower nascent O(^1D) velocity distribution (O_3 vs. N_2O photolysis) [*Thelen et al.*, 1995] and more efficient electronic quenchers (N_2/O_2 vs. He bath gas) [*Sander et al.*, 2006] in the stratosphere. In addition, minor O(^1D)-producing channels

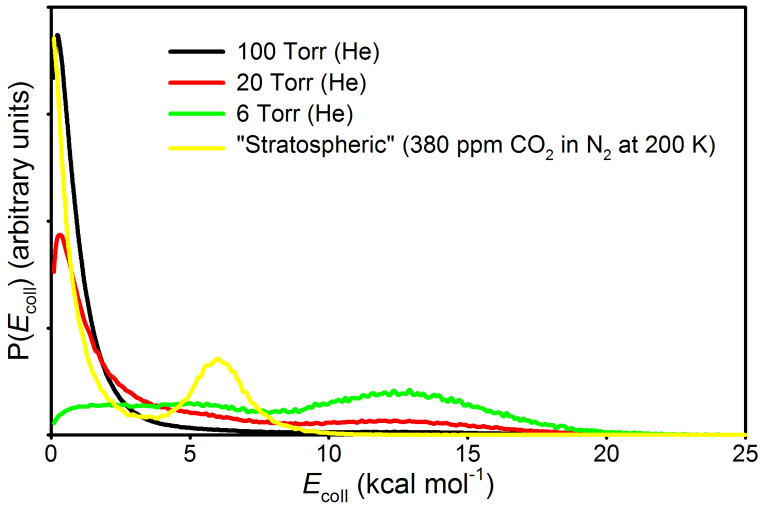

Figure 2.6: **Modeled O(^1D) + CO_2 reaction collision energy distributions at different He bath gas pressure (T = 300 K).** Also shown is the modeled $P(E_{coll})$ under conditions resembling the stratosphere, using O_3 as a source of O(^1D).

important to the stratosphere have not been included in this model (see *Taniguchi et al.* [2000]). Last, the velocity relaxation problem is only qualitatively represented by the hard-sphere model; inelastic collisions are not necessarily described well by the hard-sphere cross-sections, especially when the collision partners are diatomic, and spin-orbit coupling is important [*Kharchenko and Dalgarno*, 2004]. Thus, the "stratospheric" O(^1D) collision model results are only intended for qualitative comparison with the laboratory O(^1D)–He results.

2.5.1.4 Pulsed-photolysis results

The results of the pulsed laser experiments are plotted in Figure 2.7 and shown in Table 2.4. At both temperatures, Δ_{47} of CO_2 decreases with increasing extent of photochemical isotope exchange ($\Delta\delta^{18}O$), indicating the O(^1D) + CO_2 reaction does not selectively enrich $^{16}O^{13}C^{18}O$ relative to $^{16}O^{12}C^{18}O$. Additionally, no significant temperature dependence was observed in Δ_{47} vs. $\Delta\delta^{18}O$, as the 300 K and 229 K data are indistinguishable within our experimental uncertainty; consequently, the data were considered together in the subsequent determination of the $^{13}C/^{12}C$ KIE. The best-fit slope of the Δ_{47} vs. $\Delta\delta^{18}O$ relationship in the experimental data was calculated to be –0.0036 ± 0.0008 (2σ), corresponding to a

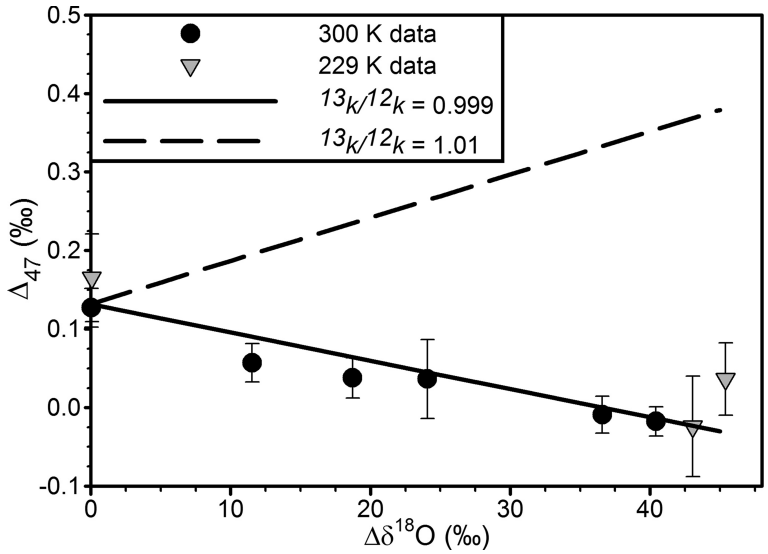

Figure 2.7: **Changes in Δ_{47} vs. $\Delta\delta^{18}$O after pulsed UV photolysis at 300 K (circles) and 229 K (triangles).** $\Delta\delta^{18}O = \delta^{18}O_{final}$ - $\delta^{18}O_{initial}$. Also shown is the modeled Δ_{47} vs. $\Delta\delta^{18}$O dependence for $^{13}C/^{12}C$ KIE = $^{13}k/^{12}k = 0.999$ and 1.01 (offset by $\Delta_{47} = +0.13$‰ for clarity; the significance of this and of the slopes is discussed in the text). Error bars represent 2σ standard errors.

Table 2.4: Results of pulsed photochemical experiments

Temperature	$\delta^{13}C$ (‰)	$\delta^{18}O_i$ (‰)	$\delta^{18}O_f$ (‰)	$\Delta\delta^{18}O^{\dagger}$ (‰)	$\Delta_{47,f}$ (‰)	$\sigma_{\Delta_{47,f}}$ (‰)
Photolysis experiments						
300 K	-10.76	29.84	66.41	36.57	-0.009	0.012
	-10.56	29.95	54.03	24.08	0.036	0.025
	-23.79	15.50	58.44	42.94	0.104	0.017
	-24.24	15.48	55.89	40.41	-0.018	0.009
	-10.69	30.08	48.79	18.71	0.038	0.013
	-10.55	29.63	41.17	11.54	0.057	0.012
229 K	-24.13	15.28	58.33	43.05	-0.024	0.032
	-25.15	14.46	59.86	45.40	0.036	0.023
Blank experiments						
300 K	-10.67	29.81	29.72	-0.09	0.150	0.011
	-19.22	20.84	20.88	0.04	0.127	0.012
229 K	-25.09	14.22	14.29	0.07	0.165	0.028

Blank experiments were run without photolysis step. $^{\dagger}\Delta\delta^{18}O = \delta^{18}O_f$ - $\delta^{18}O_i$

$^{13}C/^{12}C$ KIE of 0.999 $\pm$ 0.001 (2σ). This KIE value was obtained by modeling the $^{13}C/^{12}C$ KIE value corresponding to the best-fit slope of the Δ_{47} vs. $\Delta\delta^{18}O$ data shown in Figure 2.7 (0.999, assuming a $^{13}C/^{12}C$ KIE of 1 in reaction 2.2). Its uncertainty was estimated by varying the $^{13}C/^{12}C$ KIE until the modeled slope varied $\pm$ 0.0008; the upper and lower limits of the $^{13}C/^{12}C$ KIE (1.000 and 0.998, respectively) were then taken as the 2σ uncertainty bounds. In contrast, a $^{13}C/^{12}C$ KIE of 1.01, the KIE required to explain the polar vortex Δ_{47} vs. $\Delta^{17}O$ correlation (see Section 2.5.1.3), would yield a slope of +0.0055 in Figure 2.7. The negative experimental slope, however, rules out this $^{13}C/^{12}C$ KIE > 1 and thus a selective enrichment in $^{16}O^{13}C^{18}O$ resulting from reaction 2.1.

While this experiment was unable to isolate the $^{13}C/^{12}C$ KIEs in reactions 2.5 and 2.6, the laboratory data are consistent with the $^{13}C/^{12}C$ KIE in reaction 2.5 dominating the observed Δ_{47} vs. $\Delta\delta^{18}O$ relationship. Reactions 2.5 and 2.6 are both important in the stratosphere, with the branching ratio between them likely 9:1 (2.5:2.6) at the average stratospheric collision energy (see *Mebel et al.* [2004]) and thus also at the $\langle E_{coll} \rangle$ in our experiments. Using this branching ratio, we calculate that the experiment is approximately three times more sensitive to a $^{13}C/^{12}C$ KIE in reaction 2.5 than in reaction 2.6. A $^{13}C/^{12}C$ KIE $\sim$ 0.993 in reaction 2.6, then, is also consistent with the laboratory Δ_{47} vs. $\delta^{18}O$ slope. If the observed slope were arising exclusively from a $^{13}C/^{12}C$ KIE in reaction 2.6, it would become increasingly negative with increasing initial $\langle E_{coll} \rangle$ because reaction 2.6 is favored at higher E_{coll} [*Mebel et al.*, 2004; *Perri et al.*, 2004]. Several high-collision-energy (no buffer gas, initial $\langle E_{coll} \rangle \approx$ 13.6 kcal mol^{-1}) experiments were performed to test this hypothesis; they also showed depletions in Δ_{47} as the extent of photochemical isotope exchange increased, with no significant (i.e., factor-of-three) change in Δ_{47} vs. $\Delta\delta^{18}O$. Other combinations of $^{13}C/^{12}C$ KIEs in reactions 2.5 and 2.6 could also yield the laboratory Δ_{47} vs. $\Delta\delta^{18}O$ slope, but the absence of significant temperature and collision-energy dependence in the laboratory data, along with negligible $O(^1D)$–CO_2 association and dissociation barriers on the singlet electronic potential energy surface [*Mebel et al.*, 2004], support our attribution of the measured isotope effects to reaction 2.5. As such, we report a $^{13}C/^{12}C$ KIE of 0.999 $\pm$ 0.001 (2σ), which is within the uncertainty of a KIE of 1.000 expected for

stochastic isotope exchange.

2.5.2 Continuous-irradiation experiments

2.5.2.1 Methods

Continuous-irradiation experiments on the $O_2/O_3/CO_2$ photochemical system were performed at UC-Berkeley to examine whether the aggregate isotope effect from all $O(^1D)$–CO_2 reaction pairs would still yield depletions in Δ_{47} with increasing extent of photochemical isotope exchange. A 2 L glass reaction bulb was filled with mixtures of O_2 and CO_2 of known isotopic composition between 100 – 150 Torr total pressure at 295 K, and the mixture was irradiated between 0 – 48 hours with a pen-ray mercury lamp through a MgF_2 window. This scheme generates $O(^1D)$ through narrow-band photolysis of O_2 at 185 nm (6×10^{13} – 1.5×10^{14} photons cm^{-2} s^{-1}) and subsequent photolysis of O_3 at 254 nm (2×10^{15} photons cm^{-2} s^{-1}). Residual O_2 was separated cryogenically from the mixture, and O_3 was catalytically decomposed on hot nickel foil at 333 K for 15 minutes before the CO_2 was purified for isotopic analysis.

A commercially available software program, KINTECUS (Windows version 3.95, 2008; [*Ianni*, 2003]), was used to simulate the kinetics of the photochemical oxygen isotope exchange between O_2 and CO_2 in the continuous-irradiation experiments. The species modeled were O_2, $O_2(^1\Delta)$, $O_2(^1\Sigma_g^+)$, $O(^3P)$, $O(^1D)$, O_3, and CO_2 and included both singly- and doubly-substituted ^{17}O- and ^{18}O- isotopologues as well as ^{13}C isotopologues of CO_2, yielding more than 400 isotope-specific reactions. Rate coefficients for each reaction corresponding to all common isotopologues were from *Sander et al.* [2006], while photolysis rate coefficients (J-values) were calculated from the reported irradiance of the mercury pen-ray lamp at 254 nm [*Reader et al.*, 1996], the geometry of the bulb, and the measured cross sections of O_2 at 185 nm and O_3 at 254 nm [*Sander et al.*, 2006]. The only oxygen KIEs included in the model are in the ozone recombination reaction [*Janssen et al.*, 2001] and in O + O_2 isotope exchange [*Kaye and Strobel*, 1983; *Wiegell et al.*, 1997]. Stochastic scrambling of oxygen was assumed to occur in the $O(^1D)$ + CO_2 isotope exchange reaction [*Baulch and Breckenridge*, 1966; *Yung et al.*, 1997], and scenarios with hypothetical $^{13}C/^{12}C$ KIEs of 1,

Table 2.5: Results of continuous irradiation experiments

Sample name†	Irradiation time (h)	$\delta^{18}O$ (‰)	$\Delta^{17}O$ (‰)	Δ_{47} (‰)
Starting CO_2	0.0	6.4	0.0	1.10
ANOM 1	48.0	67.4	24.8	0.72
ANOM 1	48.0	67.4	24.8	0.85
ANOM 2	4.5	13.1	2.3	0.96
ANOM 2	4.5	13.2	2.3	1.04
ANOM 4	10.0	19.0	4.8	0.75

†Samples with the same names are replicate analyses for Δ_{47}, taken as separate aliquots of the same experiment.

0.999, and 0.998 were considered *a priori*. The model was initialized with the experimental partial pressures, temperature, and starting isotopic compositions of O_2 and CO_2.

2.5.2.2 Continuous-irradiation results

The laboratory results from the continuous-irradiation experiments are shown in Table 2.5 and compared with the modeling results in Figure 2.8. We observed a depletion in Δ_{47} with increasing $\Delta^{17}O$ (a proxy for the extent of photochemical isotope exchange), in agreement with the results from our pulsed photolysis experiments. Within the uncertainty bounds reported for the $^{13}C/^{12}C$ KIE, the continuous irradiation experiments are also generally consistent quantitatively with our pulsed photolysis experiments. There is a noticeable disagreement, however, at the largest $\Delta^{17}O$ value (48-hour irradiation time). Some of this error could be attributed to our assumptions about the initial distribution of CO_2 isotopologues in the model: The initial $\Delta_{47} > 0$ was modeled as an excess of $^{16}O^{13}C^{18}O$ exclusively, although contributions from $^{17}O^{12}C^{18}O$ and $^{13}C^{17}O_2$ may be nontrivial. In addition, trace water in the reaction bulb (in the gas phase or adsorbed onto the glass) could catalyze CO_2–water isotope exchange reactions and drive the distribution of CO_2 isotopologues towards equilibrium, i.e., $\Delta_{47} = 0.86‰$ at 298K. Both of these uncertainties would be exacerbated as the irradiation time increases, leading to a marked deviation from the modeled result at longer irradiation times. Last, the effects of the O_3 decomposition step on Δ_{47} have not been fully elucidated; previous reports have documented some oxygen isotope exchange

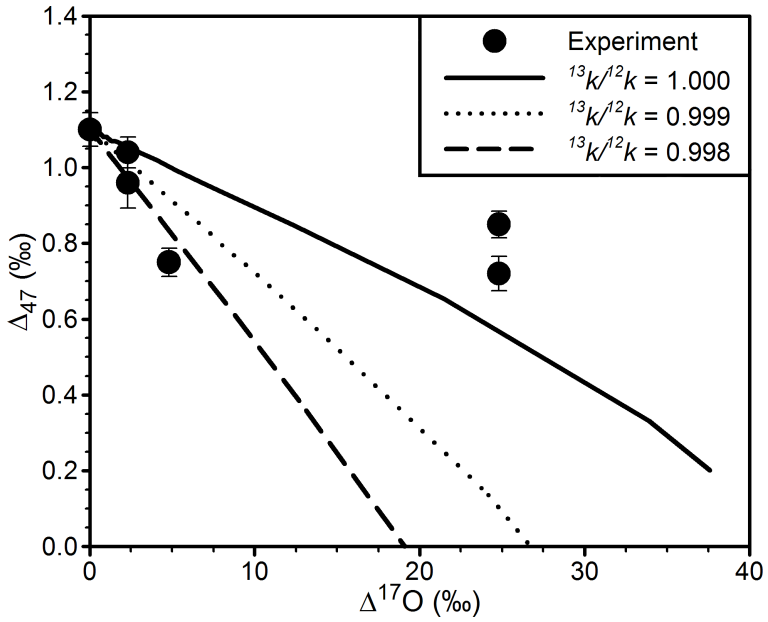

Figure 2.8: **Changes in Δ_{47} vs. Δ^{17}O of CO_2 after continuous UV irradiation of $O_2/O_3/CO_2$ mixtures with a Hg lamp.** Experimental results are compared with calculated results ($^{13}C/^{12}C$ KIE = = $^{13}k/^{12}k$ = 1, 0.999, and 0.998 obtained *a priori* from a kinetics model of the photochemical experiment. Error bars represent 2σ standard errors.

when O_3 is decomposed on hot nickel [*Johnston et al.*, 2000; *Shaheen et al.*, 2007], perhaps with the nickel oxide layer or surface-adsorbed water, so the post-irradiation O_3 decomposition step during CO_2 purification may drive Δ_{47} towards its isotopic equilibrium value ($\Delta_{47} \sim 0.8$‰ at 333 K; see *Wang et al.* [2004]) at the nickel's temperature. We performed experiments to test this hypothesis by heating O_3/CO_2 mixtures (with initial $\Delta_{47} = 0$) in the presence of nickel foil and/or powder at 88, 125, and 155°C. The resulting Δ_{47} values of CO_2 showed 1 – 2‰ changes in δ^{18}O and 0.5 – 0.6‰ increases in Δ_{47}, consistent with isotopic equilibration occurring on the nickel surface.

Still, the continuous irradiation experiments are consistent with the results of the pulsed photolysis experiments. They show that the $O(^1D)$ + CO_2 isotope exchange reaction drives the CO_2 isotopologue distribution towards a stochastic distribution.

2.5.3 Conclusions from laboratory measurements

In both sets of experiments, Δ_{47} of CO_2 decreases with increasing extent of photochemical isotope exchange, as measured by the change in δ^{18}O ($\Delta\delta^{18}$O; see Figure 2.7) or Δ^{17}O

of CO_2 (see Figure 2.8), indicating the $O(^1D)$ + CO_2 reaction does not selectively enrich $^{16}O^{13}C^{18}O$ relative to $^{16}O^{12}C^{18}O$. Furthermore, these results are consistent with a statistical oxygen isotope exchange mechanism; using the results from the ^{18}O-labeled experiments at 300 K and 229 K and the comprehensive kinetics model of the pulsed photolysis experiment, we calculated a $^{13}C/^{12}C$ KIE of 0.999 $\pm$ 0.001 (2σ est.), which is not significantly different from the KIE of 1.000 expected for statistical isotope exchange branching fractions and is quantitatively consistent with the results from the continuous irradiation experiments. Hence, our results are consistent with previous studies asserting that the $O(^1D)$ + CO_2 isotope exchange branching fractions are partitioned statistically [*Baulch and Breckenridge*, 1966; *Johnston et al.*, 2000; *Perri et al.*, 2004]. In contrast, a $^{13}C/^{12}C$ KIE of $\sim$1.01 would be required to explain the high-latitude isotopic correlations shown in Figure 2.2.

A significant Δ_{47} change due to reactions other than 2.1 and 2.2 in the $O(^1D)$–CO_2 photochemical system is unlikely. The KIEs for the other reactions (e.g., the $^{17}O^{12}C^{18}O$-producing channel, which is absent in the pulsed photolysis experiments) would need to be at least 1.01 to be of comparable importance. In addition, the Δ_{47} – $\delta^{18}O$ – $\Delta^{17}O$ covariation observed in the continuous-irradiation experiments (which included the $^{17}O^{12}C^{18}O$-producing channel; see Figure 2.8) agreed well with our laboratory model, which assumes statistical partitioning of isotope exchange products in the $O(^1D)$ + CO_2 reaction. While not all of the relative rates for the $O(^1D)$ + CO_2 isotope exchange reaction were measured directly, the agreement between the pulsed-photolysis and continuous-irradiation experiments suggests that KIEs in the other $O(^1D)$ + CO_2 reactions [e.g., $^{18}O(^1D)$ + $^{16}O^{12}C^{17}O$] are described well using statistical product partitioning in this case. Direct measurements of the other KIEs would be required to determine whether the statistical partitioning of isotope exchange products applies rigorously for all $O(^1D)$–CO_2 reactant pairs. As such, we report a $^{13}C/^{12}C$ KIE of 0.999 $\pm$ 0.001 (2σ), which is within the uncertainty of a KIE of 1.000 expected for stochastic isotope exchange.

2.6 Discussion

2.6.1 $O(^1D)+CO_2$ only explains mid-latitude $^{16}O^{13}C^{18}O$ variations

We conclude that intrinsic isotope effects in $O(^1D)$ + CO_2 isotope exchange cannot produce the elevated values of Δ_{47} observed in stratospheric polar vortex air. Instead, the statistical partitioning of isotope exchange products in the $O(^1D)$ + CO_2 reaction drives the isotopic composition of CO_2 towards a stochastic distribution, thus decreasing Δ_{47}. Indeed, the mid-latitude observations show evidence for decreasing Δ_{47} with increasing extent of photochemical isotope exchange (see Figure 2.2). As photochemical isotope exchange approaches completion (the unlikely, but instructive case in which all the oxygen atoms in CO_2 have been exchanged), the $\Delta^{17}O$ and $\delta^{18}O$ of CO_2 will approach the $\Delta^{17}O$ and $\delta^{18}O$ of $O(^1D)$ because the size of the total oxygen reservoir (i.e., O_2, O_3, etc.) is >500x that of CO_2. Concurrently, the distribution of stable isotopes will become increasingly random, so the Δ_{47} value of CO_2 will approach zero. The slope of this approach, then, reflects the integrated effective isotope composition of $O(^1D)$ with which the CO_2 molecules in the air samples have exchanged since entering the stratosphere; it is possible, however, that other terms in the stratospheric CO_2 budget (e.g., CO oxidation) may, more subtly, change the isotopic composition of CO_2 and thus the isotopic composition of $O(^1D)$ one would infer from such a trend.

We constructed a box model to calculate the effective integrated mid-latitude $O(^1D)$ isotope composition to evaluate this hypothesis quantitatively. The results of our laboratory photochemistry model ($^{13}C/^{12}C$ KIE experiments) were fit to the slope of weighted linear regressions of the mid-latitude Δ_{47} data (Figure 2.2). A quenching (reaction 2.5) and non-quenching (reaction 2.6) branching ratio of 9:1 in the isotope exchange reaction was used. Atmospheric Δ_{47} enrichments (e.g., Δ_{47} = 1.1‰) were treated as $^{16}O^{13}C^{18}O$ enrichments exclusively, since contributions to Δ_{47} from $^{17}O^{12}C^{18}O$ and $^{13}C^{17}O_2$ are $\leq$ 3%. Uncertainties in the fit $\Delta^{17}O$ and $\delta^{18}O$ values were estimated by varying $\delta^{17}O$ and $\delta^{18}O$ to match the 2σ uncertainty in the slope of the weighted linear regressions.

Using this box model and the mid-latitude observations, we estimate $\Delta^{17}O = 80.6^{+59.7}_{-24.1}$‰

and $\delta^{18}O = 98.0^{+43.7}_{-17.1}$‰ ($2\sigma$ est.) as values for the integrated effective isotopic composition of $O(^1D)$, which is consistent with ozone photolysis being the primary $O(^1D)$ source in the stratosphere. While the $\delta^{18}O$ of $O(^1D)$ we calculate is similar to that found in low- and mid-latitude stratospheric ozone, $\Delta^{17}O$ is larger, on average, by 35‰ [*Krankowsky et al.*, 2007]. This is expected because $\Delta^{17}O$ enrichments in ozone are concentrated at terminal atom positions [*Michalski and Bhattacharya*, 2009]; when ozone is photolyzed to $O(^1D)$ and O_2, one of the terminal atoms is ejected [*Dylewski et al.*, 2001], elevating the proportion of heavy oxygen isotopes in $O(^1D)$. We note that the upper and lower uncertainty limits of the reported $\Delta^{17}O$ and $\delta^{18}O$ values are correlated; they correspond to fits that simultaneously match the upper and lower uncertainty limits of the mid-latitude Δ_{47} vs. $\Delta^{17}O$ and Δ_{47} vs. $\delta^{18}O$ weighted linear regressions. They reflect spatial and temporal variations in $O(^1D)$ isotope composition expected to be caused by variations in ozone concentrations, temperature, pressure, actinic flux, and various mass-dependent kinetic and photolytic isotope effects that depend on these variables.

2.6.2 Effects of intra-stratospheric chemistry and mixing

Having experimentally excluded intrinsic isotope effects in the $O(^1D)$ + CO_2 isotope exchange reaction as the source of high stratospheric Δ_{47} in polar vortex air, we consider the possible effects of other gas-phase stratospheric processes on the CO_2 isotopologue budget. CO is produced in the stratosphere by CH_4 oxidation and destroyed with an e-folding time of about two to three months by reaction with OH radicals to form CO_2. We estimate that up to 0.9 ppmv CO_2 could be derived from CH_4 oxidation in our samples based on the difference between the observed CH_4 concentrations (Table 2.1) and the average CH_4 concentration in air entering the stratosphere from the troposphere (1.7 ppmv). $^{12}C/^{13}C$ KIEs for CH_4 + OH, CH_4 + $O(^1D)$, and CH_4 + Cl of 1.004, 1.01, and 1.07, respectively [*Brenninkmeijer et al.*, 2003], should yield ^{13}C-depleted CH_3 radicals at all latitudes, particularly in the polar vortex, where Cl levels are elevated. CH_3 radicals then undergo several rapid oxidation steps to form formaldehyde (CH_2O). Isotope effects in CH_2O photolysis to form CO also favor the light isotopologues [*Feilberg et al.*, 2005a]. These isotope effects, com-

bined with expected ^{13}C compositions for stratospheric CH_4 in these samples ($\delta^{13}C$ = –47 to –35‰) should produce CO that is depleted in ^{13}C relative to background stratospheric CO_2. Small inverse $^{12}C/^{13}C$, $^{16}O/^{18}O$, and $^{16}C/^{17}O$ KIEs (i.e., < 1) in the reaction CO + OH to form CO_2 at low pressures [*Röckmann et al.*, 1998] imply that, in principle, CO + OH reactions could increase Δ_{47} values in the product CO_2, while at higher pressures, the CO + OH reaction yields ^{13}C-, ^{18}O-, and ^{17}O-depleted CO_2 [*Feilberg et al.*, 2005b]. Ultimately, however, the size of Δ_{47} values in the $\leq$ 0.9 ppmv CO_2 derived from CH_4 oxidation would likely be orders of magnitude too small to increase Δ_{47} values significantly in the other $\sim$365 ppmv of background stratospheric CO_2. A possibility remains that unusual timing in the competition between oxidation and photolysis of species in the polar vortex, combined with unexpectedly large carbon and oxygen KIEs in some Cl and Br reactions (e.g., Br + CH_2O; see *Feilberg et al.* [2004]) or other gas-phase processes might be responsible for the mid-latitude-polar vortex differences in Δ_{47} given the large differences in Cl and Br concentrations in polar vortex vs. mid-latitude air, but this seems unlikely in light of the known chemistry and KIEs.

Expected changes in $\delta^{18}O$ and $\delta^{17}O$ due to intra-stratospheric mixing are also too small to yield highly enriched polar vortex Δ_{47}. Effects of CO_2 sources on Δ_{47} can be calculated by solving the three-end-member mixing problem between (*1*) tropospheric CO_2, (*2*) stratospheric CO_2 undergoing photochemical isotope exchange, and (*3*) stratospheric CO_2 derived from a third source and accounting for the non-linearity in mixing (see Appendix 2.A). Therefore, we constructed a mixing model to simulate the effects of mixing isotopically distinct CO_2 sources on stratospheric air. The tropospheric end-member was given an isotopic composition equal to measured 'clean' troposphere values (based on measurements of air sampled from Barrow, Alaska, and Cape Grim, Tasmania; see *Affek et al.* [2007]), namely, $\delta^{13}C_{trop}$ = –8‰, $\delta^{18}O_{trop}$ = 41‰, $\delta^{17}O_{trop}$ = 21‰, and Δ_{47trop} = 0.92‰. Unfortunately, no measurements of Δ_{47} in the tropical troposphere exist, so Δ_{47trop} of the air entering the stratosphere from the tropics is uncertain. The mid-latitude Δ_{47} vs. $\Delta^{17}O$ relationship implies that Δ_{47} may be as high as 1.09‰, but changes of Δ_{47trop} on this order do not affect our qualitative understanding of mixing on stratospheric Δ_{47}. The stratospheric end-

member was $\delta^{13}C_{strat}$ = –8‰, $\Delta^{17}O$ = 80.6‰, and $\delta^{18}O$ = 98.0‰; this was our integrated effective isotopic composition for $O(^1D)$ calculated from the mid-latitude Δ_{47} variations.

We find that two-component mixing between tropospheric and stratospheric air masses does not exhibit sufficient non-linearity to generate the observed Δ_{47} enrichments in high-latitude samples. Mixing non-linearities in Δ_{47} increase as the bulk isotope compositions of the two end-members become more dissimilar, but stratospheric $O(^1D)$–CO_2 isotope exchange alone cannot produce a CO_2 mixture of sufficiently high Δ_{47}. For instance, mixing effects generate Δ_{47} changes < 0.1‰ in the troposphere [*Eiler and Schauble*, 2004], where bulk isotope compositions of major constituents of the CO_2 budget vary typically $<$ 20‰ [*Affek et al.*, 2007; *Ciais and Meijer*, 1998]. A mixture of tropospheric CO_2 and mid-latitude stratospheric CO_2 would generate a similar enrichment because their bulk isotope compositions differ by a similar amount. Even in the extreme case of $\delta^{18}O_{strat}$ = 146‰, $\delta^{17}O_{strat}$ = 142‰ and $\Delta_{47strat}$ = 0‰, the oxygen isotope composition of CO_2 when it is at isotopic equilibrium with excess O_3 (an unlikely case, but an ultimately useful one in illustrating this point; see *Shaheen et al.* [2007]), two-component mixing would yield a maximum Δ_{47} change more than an order of magnitude smaller than, and in the opposite direction of, that which is observed in polar vortex samples over the same range in $\Delta^{17}O$. Bulk isotope compositions of the two CO_2 reservoirs must differ in $\delta^{18}O$ and/or $\delta^{13}C$ by orders of magnitude not previously observed in the stratosphere to generate Δ_{47} enrichments of $\sim$0.7‰ observed in polar vortex samples.

2.6.3 Effects of mesospheric and heterogeneous chemistry

Physical or chemical processes in the mesosphere may yield extreme isotopic enrichments in CO_2 or CO such that subsidence of mesospheric air into the 1999/2000 stratospheric polar vortex [*Plumb et al.*, 2003] could explain the observed meridional variation in Δ_{47}. Thus, we will next consider three mesospheric processes that have been previously studied in other contexts: Gravitational separation of upper atmospheric air, UV photolysis of O_2, and UV photolysis of CO_2.

2.6.3.1 Mixing of gravitationally separated air into the stratosphere

Gravitational separation can concentrate heavy isotopologues of CO_2 into the lower mesosphere [*Ishidoya et al.*, 2008], which could elevate stratospheric Δ_{47} values after mesospheric subsidence and mixing. The expression in Craig [*Craig et al.*, 1988] for the enrichment of a species N_i versus a second species N in per mil is based on the kinetic theory of gases [*Gibbs*, 1948]:

$$\Delta\left(\frac{N_i}{N}\right) = \Delta M \frac{gZ}{RT} \times 10^3 \tag{2.8}$$

where ΔM is the difference in mass, g is the acceleration due to gravity (9.81 m s^{-2}), Z is the column length, R is the gas constant, and T is the temperature. Using a reasonable column length of 50 km at a temperature of 220 K, gravitational separation of CO_2 would increase $\delta^{13}C$, $\delta^{18}O$, and $\delta^{17}O$ by 266‰, 6223‰, and 1113‰, respectively, but would lead to a *decrease* in Δ_{47} by 74‰ at the bottom of the column. In addition, polar vortex $\delta^{13}C$ is not markedly more enriched from mid-latitude $\delta^{13}C$, implying that gravitational separation is generally negligible for the samples in this study.

2.6.3.2 Mixing of mesospheric air highly enriched in ^{17}O and ^{18}O

Isotope effects in the photolysis of O_2 by short-wavelength UV radiation in the upper mesosphere might lead to unusually enriched CO_2 in the mesosphere. *Liang et al.* predicted recently that differences in photolysis cross-sections between light and heavy isotopologues of O_2 in the narrow solar Lyman-α region (121.6 nm) may result in a population of mesospheric $O(^1D)$ enormously enriched in ^{17}O and ^{18}O [*Liang et al.*, 2007]. This extreme enrichment in $O(^1D)$ could then be transferred to mesospheric CO_2 through the $O(^1D)+CO_2$ isotope exchange reaction. CO_2 photolysis in the mesosphere to form CO, followed by oxidation of that same CO by OH in the polar vortex, might also significantly affect the Δ_{47} values of CO_2 in the polar vortex.

To evaluate the effects of ^{17}O- and ^{18}O-enriched mesospheric CO_2 mixing into the stratospheric polar vortex, we constructed a three-component mixing model that included air

Table 2.6: Tropospheric-stratospheric-mesospheric mixing model results

Sample name	f^*_{trop}	f_{strat}	f_{meso}	$\delta^{18}O_{strat}$ (‰)	$\delta^{18}O_{meso}$ (‰)	$\delta^{18}O$ (‰)	$\Delta^{17}O$ (‰)	Δ_{47} (‰)
						Mixing model results		
20000312(25)1120	0.925	0.075	2.6×10^{-6}	82.5	1.76×10^5	44.55	5.76	1.614
20000131(30)1001	0.943	0.057	2.1×10^{-6}	80.0	1.86×10^5	43.62	4.38	1.555
20000203(10)1173	0.952	0.048	1.4×10^{-6}	77.7	2.07×10^5	43.06	3.69	1.436
20000127(5)1060	0.967	0.033	1.7×10^{-6}	87.9	1.47×10^5	42.79	2.45	1.233

*Mixing fraction of tropospheric air, calculated as $1 - f_{strat} - f_{meso}$.

mass contributions from the troposphere, stratosphere, and mesosphere. Each polar vortex datum (i.e., with unique $\Delta^{17}O$, $\delta^{18}O$, and Δ_{47} values) was fit individually because of the presence of mesospheric filaments in the polar vortex [*Plumb et al.*, 2003] and consequent heterogeneity in the mixing fraction and end-member isotopic composition between samples. The multiply-substituted isotopologue distribution was fixed at $\Delta_{47meso} = 0$ for this simple mixing-only scenario because our kinetics experiments and the mid-latitude stratosphere Δ_{47} values indicate that isotope exchange drives the isotopologue distribution towards a stochastic one. No measurements of mesospheric $\delta^{13}C$ exist, so $\delta^{13}C_{meso} = -8‰$ was used; however, the calculated enrichment in mesospheric $\delta^{18}O$ was insensitive to the choice of $\delta^{13}C$.

We were unable to reproduce the polar vortex data in both bulk isotope compositions and Δ_{47} simultaneously when using the mesospheric ^{18}O and ^{17}O enrichments in CO_2 mixing end-member suggested by *Liang et al.* [2007] (i.e., $\delta^{18}O = 10{,}603‰$, $\delta^{17}O = 3{,}149‰$, and $\Delta_{47} = 0$). Only after $\delta^{18}O$ and $\delta^{17}O$ of the mesospheric CO_2 end-member were increased an additional tenfold (i.e., $\delta^{18}O \sim 10^5‰$ and $\delta^{17}O \sim 10^4‰$) were the Δ_{47} – $\delta^{18}O$ – $\Delta^{17}O$ systematics of the polar vortex samples reproduced. Modeled mixing fractions (f_{trop}, f_{strat}, and f_{meso}) and isotopic compositions for each of the high-latitude CO_2 samples are given in Table 2.6.

Due to the uncertainty in our calculated $\Delta^{17}O_{strat}$ and $\delta^{18}O_{strat}$ values (see Section 2.6.1), $\delta^{18}O_{strat}$ was allowed to vary freely about our estimate above; the resulting $\delta^{18}O_{strat}$ values generally fell within the range we predicted. The combined uncertainties introduced by our calculated mid-latitude $O(^1D)$ isotope composition and the other parameters used in these

fits suggest that these results are likely only meaningful to within an order of magnitude.

No laboratory measurements of the isotopic fractionations in O_2 due to Lyman-α photolysis are available to compare with our modeled isotopic compositions, however. Because the Lyman-α lines fall on the edge of the $\tilde{E}^3\Sigma_u^- \leftarrow \tilde{X}^3\Sigma_g^-$ (1,0) absorption band of O_2, a small absolute absorption cross-section error for one O_2 isotopologue can translate into a significant isotopic fractionation error. Relaxing the mesospheric $\delta^{18}O$ vs. $\delta^{17}O$ relationship predicted by *Liang et al.* [2007], i.e, $\delta^{17}O = 0.3 \times \delta^{18}O$, increases the modeled $\delta^{18}O_{strat}$ values and lowers the predicted $\delta^{18}O_{meso}$ values, but the mesospheric CO_2 mixing end-member is still enriched overall to ~100,000‰ in $\delta^{18}O$ and $\delta^{17}O$. A simple calculation (assuming 365 ppm CO_2 and an initial $\delta^{18}O = 23.5$‰ in O_2) predicts that the mesospheric O_2 end-member should have a $\delta^{18}O$ value on the order of –100‰. Furthermore, we note that the $O(^1D)$ + CO_2 reaction may not necessarily partition products statistically (i.e., drive $\Delta_{47} \rightarrow 0$) in the mesosphere, as we assumed here, because the average collision energy there is higher than in the stratosphere.

In principle, measurements of the isotopic composition of mesospheric CO should constrain the isotopic composition of mesospheric CO_2 downwelling into the polar vortex. Large elevations in CO above background stratospheric levels, observed at high altitudes in the polar vortex [*Plumb et al.*, 2003], are due to CO_2 photolysis in the mesosphere and subsequent transport to the stratosphere, so the isotopic composition of CO in these cases should reflect that of the mesospheric CO_2 population and any fractionations arising from CO_2 photolysis there. The bulk isotope composition in mesospheric CO_2 predicted by our three-component mixing model (e.g., tens of percent in ^{18}O-atom abundance, or 100x natural abundance) would result in isotopic enrichments in mesospheric CO that are detectable with remote-sensing spectrometers because CO_2 photolysis isotope effects are expected to be much smaller in magnitude. For example, *Bhattacharya et al.* [2000] measured fractionations of ~100‰ in ^{17}O and ^{18}O in their UV-photolysis experiments; CO_2-photolysis fractionation in the mesosphere could be larger, but the wavelength dependence of these across the actinic spectrum is difficult to estimate because the physical origin of the laboratory fractionations is not understood (see below). Remote-sensing measurements by the JPL

MkIV Fourier-transform spectrometer, however, does not show hundred-fold enrichments in ^{18}O of mesospheric CO observed downwelling to 30 km altitude in the polar vortex (G. C. Toon, personal communication, 2009). On the basis of this observation, mesospheric CO_2 does not appear to possess oxygen isotopic enrichments of sufficient size to produce high Δ_{47} values in the polar vortex upon mixing with stratospheric air masses, although the long path-length and consequent averaging over mesospheric filaments and background stratospheric air of the MkIV instrument will dilute any mesospheric signal. Remote sensing of CO and/or CO_2 isotopologue abundances in the mesosphere are thus needed to constrain this hypothesis.

2.6.3.3 Oxidation of mesospheric CO in the polar vortex

Next, we examine the potential impacts of mesospheric CO_2 photolysis to form CO, followed by mixing and re-oxidation into CO_2, on polar vortex Δ_{47} values. The photolysis of CO_2 in the UV region may result in wavelength-dependent isotope effects, although this contention is based on a single laboratory measurement. *Bhattacharya et al.* [2000] performed laboratory experiments in which they photolyzed CO_2 with either a Kr lamp (120 – 160 nm) or a Hg lamp (185 nm) and measured the ^{17}O and ^{18}O compositions of the product CO and O_2. The 120 – 160 nm results suggest that mass-dependent depletions of order 50‰ and 100‰ in ^{18}O and ^{17}O of CO, respectively, are possible, which would enrich the remaining CO_2 reservoir in ^{18}O and ^{17}O. The 185-nm results were quite different: Photolysis of CO_2 near natural isotopic abundance showed mass-independent enrichments in ^{17}O up to 150‰ with little change in ^{18}O in the CO and O_2 products, while photolysis of ^{13}C-labeled CO_2 showed mass-dependent enrichments in ^{18}O and ^{17}O in the ^{13}CO and O_2 products of $\sim$50 and 100‰, respectively. Taken alone, these latter isotope dependences could result in mesospheric CO that is significantly enriched in ^{18}O, ^{17}O, and ^{13}C, and perhaps even $^{13}C^{18}O$. The remaining mesospheric CO_2 would be correspondingly depleted in heavy isotopologues.

If similar isotopic fractionations occur in CO and CO_2 when CO_2 is photolyzed by UV radiation in the mesosphere, then the population of mesospheric CO downwelling into the

stratospheric polar vortex could have a large impact on the Δ_{47} values of CO_2 in the polar vortex. Once in the stratosphere, mesospheric CO will be oxidized by OH to produce CO_2 in the polar vortex. Oxidation of this CO could, in principle, contribute to the large polar vortex values of Δ_{47} in CO_2 observed because: (*1*) CO mixing ratios as large as 10 ppmv have been observed in mesospheric filaments in the stratosphere (a thousand-fold higher than background stratospheric CO abundances in the polar vortex) [*Plumb et al.*, 2003], (*2*) the known KIEs for the CO + OH reaction are expected to favor formation of $^{13}C^{18}O$-containing CO_2 molecules in the stratosphere [*Feilberg et al.*, 2005b; *Röckmann et al.*, 1998], and (*3*) the lifetime of CO with respect to oxidation is several months, and is therefore not immediately quantitative. These three phenomena could result in a sub-population of CO_2 with elevated concentrations of $^{16}O^{12}C^{17}O$, $^{16}C^{12}C^{18}O$, and $^{16}C^{13}C^{18}O$ (or other mass-47 isotopologues of CO_2), given the sign and magnitude of known KIEs for the CO + OH reaction [*Feilberg et al.*, 2005b; *Röckmann et al.*, 1998]. The slow oxidation of CO may only produce temporary increases of heavy-isotopologue abundances, as large fractionations due to KIEs will decrease in magnitude as CO oxidizes quantitatively to CO_2. Measurements of the $^{13}C^{18}O$ + OH vs. $^{12}C^{18}O$ + OH KIE by *Feilberg et al.* at 298K and 1 atm suggest that the oxidation of mesospheric CO alone could account for elevated Δ_{47} in the stratospheric polar vortex [*Feilberg et al.*, 2005b]. Consequently, CO_2 photolysis in the mesosphere, followed by oxidation of the product CO in the mesosphere and/or stratosphere, may allow the heavy oxygen and carbon isotopes in CO_2 to 'reorganize' in a manner that could elevate Δ_{47} values of CO_2 in the polar vortex. The mixing of the remaining (unphotolyzed) mesospheric CO_2 with stratospheric CO_2 in the polar vortex, however, may have the opposite effect on Δ_{47} values of CO_2. Measurements of all the relevant KIEs of CO + OH reaction at stratospheric temperatures and pressures and a model of the oxidation of mesospheric CO in the stratospheric polar vortex will be required to evaluate the impact of this mechanism quantitatively.

The full impact of this mechanism is not well-constrained, however, because (*1*) the isotopic composition of mesospheric CO_2 has not been measured, (*2*) not all the KIEs for the CO + OH reaction are known at the relevant temperatures and pressures, and (*3*) the

physical origin of the photolytic fractionations associated with CO_2 photolysis are not understood. The first two points were discussed earlier, so they will not be discussed here. For the physical origin of the photolytic fractionations associated with CO_2 photolysis, *Bhattacharya et al.* suggested that dissociation rates for certain CO_2 isotopologues could be enhanced if their excited vibrational states (which get populated when the molecule absorbs UV light) overlap sufficiently with the vibrational states of another CO_2 electronic state. This would facilitate conversion of the electronically excited species $CO_2(^1B_2)$, which is promoted from ground-state CO_2 when it absorbs UV light and does not have enough energy to dissociate into O + CO under the experimental conditions, into the electronically excited species $CO_2(^3B_2)$, which does have enough energy to dissociate. If this mechanism is a general feature of the dynamics of CO_2 photodissociation, it could lead to additional mass-independent fractionations at wavelengths other than at 185 nm. Unfortunately, this hypothesis has not been tested at other wavelengths yet, and without a firm theoretical understanding, or at least an empirical wavelength dependence, of the isotopic fractionations associated with CO_2 photolysis, convolving the 120 – 160 nm results with the 185 nm results from *Bhattacharya et al.*'s experiments, and then convolving those with the actinic flux to make a prediction for Δ_{47} of mesospheric CO and CO_2 is not possible.

2.6.3.4 Heterogeneous chemistry on stratospheric particles

Finally, we consider the potential role stratospheric particles could play in the stratospheric CO_2 isotopic budget. Oxygen isotope exchange on particle surfaces could drive the population of CO_2 towards isotopic equilibrium by catalyzing CO_2–CO_2 isotope exchange reactions (e.g., $^{16}O^{12}C^{18}O + ^{13}C^{16}O_2 \rightleftharpoons {}^{12}C^{16}O_2 + {}^{16}O^{13}C^{18}O$) that are too slow to occur in the gas phase under stratospheric conditions. Zero-point energy isotope effects dominate in these reactions at equilibrium, driving the Δ_{47} value towards its equilibrium value at a given temperature. We calculate that Δ_{47} adopts a value of 1.6‰ if 70% of the CO_2 molecules achieve isotopic equilibrium at temperatures coincident with PSC formation in the polar vortex, $\sim$190 K [*Wang et al.*, 2004] . Thus, in principle, particle-catalyzed equilibration of CO_2, perhaps via CO_2 hydration reactions in quasi-liquid films at the surface of ice particles

[*Dash et al.*, 2006], could produce the observed polar vortex Δ_{47} values. Bulk isotopic compositions would be little-affected by these isotope exchange reactions, consistent with the data presented in Table 2.1 and Figure 2.2, if the catalyst reservoir (e.g., liquid water layers on a surface) is much smaller than the CO_2 reservoir; CO_2 would impart its bulk isotopic composition on the catalyst while the multiply-substituted isotopologue distribution in CO_2, which is insensitive to the isotopic composition of the catalyst, approaches that at isotopic equilibrium. However, CO_2–liquid water isotope exchange may not occur quickly enough at low temperatures and low pH to be the relevant process. Last, we note that, in order for this PSC-catalyzed isotope-exchange mechanism to explain the polar vortex Δ_{47} measurements, the mechanism must result in a strong anti-correlation with N_2O mixing ratios (Figure 2.2a); this would imply that transport is fast compared to isotope exchange on the PSCs, whose distributions are highly variable in space and time in the polar vortex. Future 2-D modeling efforts will examine whether such a mechanism remains consistent with the observations or whether transport and mixing of a mesospheric isotope signal into the polar vortex better explains the observed anti-correlation of Δ_{47} with N_2O.

We conducted preliminary experiments on the kinetics of isotope exchange on PSC-like surfaces (e.g., $H_2SO_4/HNO_3/H_2O$ mixtures; see *Molina et al.* [1993]) to test the PSC-isotope-exchange hypothesis. PSCs made from HNO_3:H_2O mixtures, i.e. 'Type Ia' PSCs, were tested first because they were a major component of the PSCs formed during the 1999/2000 Arctic winter [*Voigt et al.*, 2000] and their crystallization has been studied in the laboratory [*Hanson and Mauersberger*, 1988]. 50% HNO_3 in H_2O was crystallized at 197 K using an ethanol/dry ice bath according to the protocol outlined by *Hanson and Mauersberger* [1988]; the crystal structure and stoichiometry of the ice was not measured. Pure CO_2 of known isotopic composition was then exposed to the HNO_3 ice for 3 hours in a glass reaction vessel held at 197 K. No change in the Δ_{47} values were observed (within statistical uncertainty). Based on the volume of the reaction vessel and the amount CO_2, the root-mean-square (RMS) displacement was 2.5 cm s^{-1}. This RMS displacement was significant compared to the 15-cm length of the reaction vessel; therefore, the reaction's progress was probably not hindered by diffusion. The same experiment was performed also

with 1:1:1 H_2SO_4:HNO_3:H_2O mixtures (similar to 'Type Ib' PSCs) at 197 K, and no isotope exchange was observed in those experiments, either.

These preliminary results imply that CO_2 isotope exchange on PSCs is slow at stratospheric temperatures, although the chemical composition of the surfaces generated in the laboratory may have been different from those of real PSCs. Future studies should explore the isotope exchange reaction on all known PSC surfaces (e.g., types Ia, Ib, and II; see *Zondlo et al.* [2000] and *Prenni and Tolbert* [2001]) and assign upper limits to their rates.

2.7 Conclusions

The signature of a new process preserved in stratospheric $^{16}O^{13}C^{18}O$ proportions reveals that a second mechanism, in addition to the $O(^1D)$ + CO_2 isotope exchange reaction, alters the isotopic composition of stratospheric CO_2 and thus the interpretation of its chemical and transport 'history.' This second mechanism, which elevates Δ_{47} values in the polar vortex, is likely of either mesospheric photochemical or heterogeneous origin. To constrain further the role of each of these mechanisms, isotopic fractionations due to broadband UV photolysis of O_2 and CO_2, the KIEs of the CO + OH reaction under stratospheric conditions, and the kinetics of CO_2 isotope equilibration on the surfaces of PSCs and other stratospheric aerosols need to be studied experimentally. Additionally, kinetic and photolysis-induced isotope effects that may affect CO and CO_2 should be incorporated into atmospheric models to quantify their contributions to both the bulk and multiply-substituted isotopologue budgets of stratospheric CO_2, whose influence on the isotopologue budgets of tropospheric CO_2 may be significant.

2.8 Acknowledgements

We thank R. Lueb for whole-air-sampler and cryogenic whole-air-sampler field support, Y. L. Yung, G. A. Blake, and P. O. Wennberg for manuscript comments, and financial support from the Davidow Fund, the National Science Foundation, the NASA Upper Atmosphere Research Program. K. A. B. was supported by the Camille Dreyfus Teacher-Scholar Award.

Appendices

2.A Mixing effects on isotopic composition

The effects of CO_2 air parcel mixing on isotopic composition have specific relevance for Δ_{47} in Chapter 2, so an example follows below. In general, mixing of two or more reservoirs of CO_2 is linear in $\delta^{13}C$, $\delta^{18}O$, and $\delta^{17}O$ (the mixture has δ-value in between that of the two mixing end-members) because the references against which they are compared are constant (see Eqs. 1.5 and 1.6) Mixing of two reservoirs with the same Δ_{47} and differing bulk isotope distributions, however, can yield Δ_{47} values in the mixture different from those in the end-member gases. This nonlinear dependence of Δ_{47} on mixing arises because both R^{47}_{sample} and the reference against which it is measured ($R^{47}_{\text{stochastic}}$) change upon mixing; the reference is defined by, and therefore varies with, the bulk stable isotope ratios of that mixture. In contrast, the references used in bulk stable isotope measurements are external standards whose values are constant (e.g., VSMOW), so the bulk isotope ratios vary linearly with mixing. The degree of nonlinearity in Δ_{47} is a function of the differences in bulk isotopic composition between the mixing end-member reservoirs and their mixing fractions [*Affek and Eiler*, 2006; *Eiler and Schauble*, 2004].

Because Δ_{47} depends non-linearly on mixing fraction, even for two CO_2 reservoirs with similar Δ_{47} [*Affek and Eiler*, 2006; *Eiler and Schauble*, 2004], mixing relationships are often counterintuitive. An illustrative example is shown in Figure 2.9: The two mixing end-members (given as the bottom-left and bottom-right corners) have different initial $\delta^{18}O$ and $\delta^{17}O$ values, though both have $\delta^{13}C$ = –8‰ and Δ_{47} = 0.92‰. The concentration of $^{47}CO_2$ (i.e., R^{47}_{mix}) varies linearly with mixing fraction, but the stochastic distribution for $^{47}CO_2$ molecules also changes, varying as $\sim 2R^{13}R^{18}$. Consequently, mixing these two isotopically dissimilar CO_2 reservoirs yields a $\Delta_{47\text{mix}} > 0.92$‰ despite each reservoir being initially at Δ_{47} = 0.92‰. This type of relationship is general, and so holds for all Δ_{47}; the sign and magnitude of the resulting Δ_{47} change will depend on the end-member bulk and clumped isotope compositions.

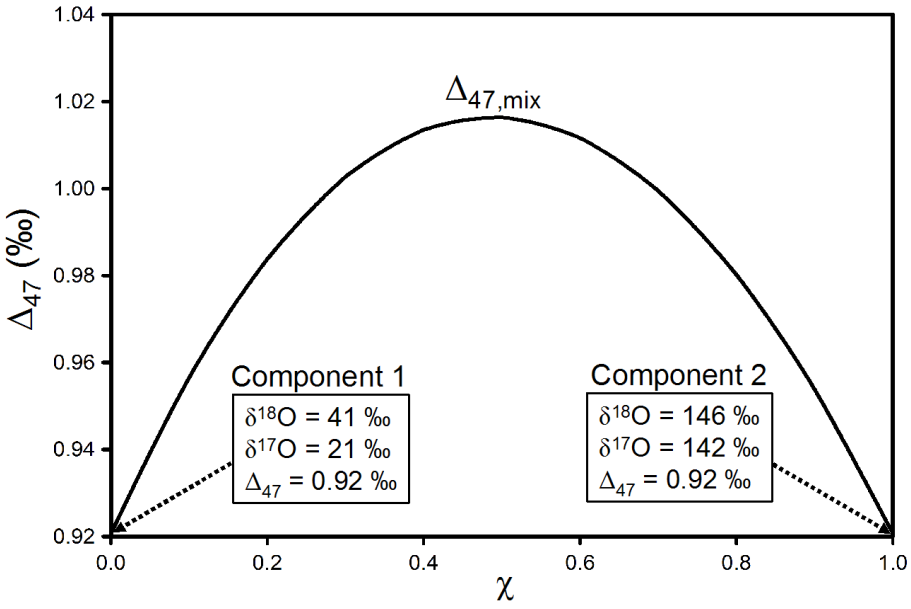

Figure 2.9: **How mixing two arbitrary reservoirs of CO_2 can be nonlinear in Δ_{47}.** The resulting mixture is more enriched in $^{47}CO_2$ relative to its stochastic distribution, as compared to either of the mixing end-members. The isotopic compositions used in this plot are for illustration purposes only; qualitatively similar effects will apply for all mixing relationships.

2.B Practical considerations

2.B.1 IRMS long-term signal stability

Δ_{47} measurements currently take ~4 hours of instrument averaging time per sample analysis. We examined the stability and accuracy of our IRMS system over this time period by using a modified form of the Allan variance technique, originally developed to characterize ultrastable oscillators [*Allan*, 1987]. Instead of using time as the independent variable, here we use individual IRMS acquisitions x:

$$\sigma^2_{\text{Allan}}(x) = \frac{1}{2(N-1)} \sum_i [\langle x \rangle_{i+1} - \langle x \rangle_i]^2 \tag{2.9}$$

Data are first binned into N bins (each consisting of one or more acquisitions), and the average of each bin, $\langle \text{x} \rangle_i$, is taken. The difference between adjacent bins is squared and then summed before being normalized to compute the Allan variance. For example, a data set with six elements [x_1, x_2, x_3, x_4, x_5, x_6] will produce three values of Allan variance corresponding to bins of one ([x_1], [x_2], [x_3], [x_4], [x_5], [x_6]), two ([x_1, x_2], [x_3, x_4], [x_5, x_6]) and three ([x_1, x_2, x_3] and [x_4, x_5, x_6]) elements each. The maximum bin size is therefore half the total number of elements in a data set.

Plotting Allan variance versus bin size, then, conveniently presents both noise- and drift-related effects on single plot. An example of the Δ_{47} Allan variance for a relatively long-duration analysis, consisting of 40 acquisitions of 80 s sample integration each (ten 8 s cycles), is shown in Figure 2.10. An ideal statistical-noise-limited measurement, for which long-term drifts are negligible, will display a power-law relationship $\sigma^2 = Cx^\alpha$ in the Allan variance plot, where α = –0.5, reflecting the Poisson statistics governing the precision of the overall measurement. In contrast, a measurement dominated by long-term, correlated random-walk drifts will have α = 0.5. Consequently, the optimum number of measurements to average together in a given analysis (i.e., the optimum bin size) will occur near where the Allan variance reaches a minimum, i.e. where $d\alpha/dx = 0$. For our instrument, measurements seem to be dominated by statistical noise for $N < 10$ acquisitions, with only a small contribution from long-term drift. The variability of σ^2 appears to increase for

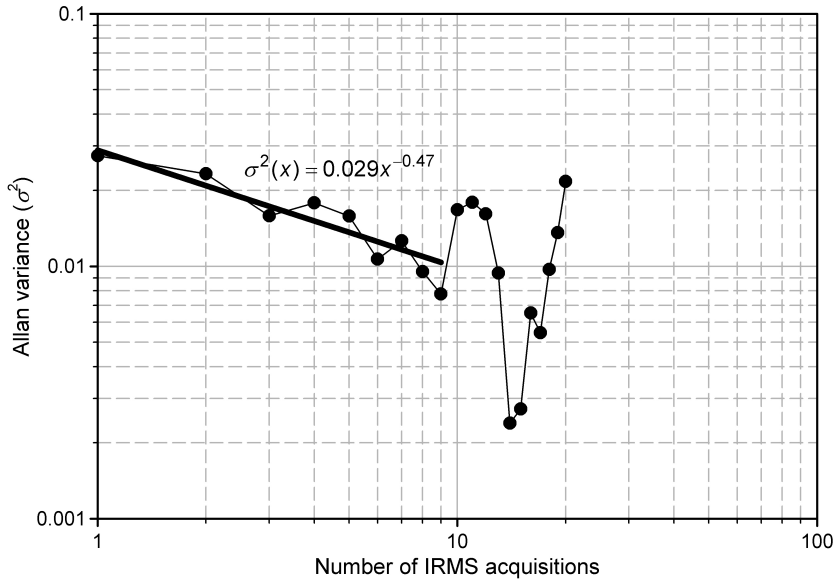

Figure 2.10: **Allan-variance plot of Δ_{47} over 40 IRMS acquisitions.** A power-law regression is shown for bins up to nine acquisitions. α = –0.47 was obtained, indicating that Poisson statistics, not long-term drifts, dominate the uncertainties in the measured Δ_{47} value in this range.

measurements made in excess of nine acquisitions (see Figure 2.10), although we attribute this to the smaller number of bins with greater than nine acquisitions contributing to the Allan variance calculation. More precise values of the Allan variance with these numbers of acquisitions would require a more sustained analytical run by several factors in time. Nevertheless, the ideal precision that should be attainable on a single gas run for measurements that are clearly dominated by statistical noise (nine acquisitions, or 720-s counting time) at the optimal voltage (16 V) is 0.013‰.

2.B.2 IRMS vs. optical methods

The best high-precision isotope-ratio measurements have been made routinely on gas-source mass spectrometers based on Nier's original 1947 design [*Nier*, 1947]. These instruments are fundamentally sensitive to that which makes stable isotopes unique — their mass — so IRMS continues to be the technique-of-choice used for stable isotope abundance measurements. It achieves high precision over a large dynamic range by utilizing multiple Faraday cups with differing amplifier gains (over a factor of 3000 for Δ_{47} measurements)

and rapid sample-standard comparison. However, the relatively poor mass-resolving power ($M/\Delta M \sim 500$) that comes as a consequence of using a magnetic sector and high-sensitivity, electrically stable Faraday-cup detectors leads to well known isobaric (same-nominal-mass) interferences, e.g., between $^{13}CO_2$ and $^{16}O^{12}C^{17}O$ at $m/z = 45$. In 'clumped' isotopologue measurements of CO_2, isobars and other impurities (e.g., N_2O, hydrocarbons) are especially important given the low absolute abundance of $m/z = 47$ isotopologues. A new concern also arises in the study of 'clumped' isotopologues: ion recombination after electron-impact ionization source can alter the measured distribution of stable isotopes vs. that present in the original sample. High-resolution and thermal-ionization mass-spectrometric techniques can potentially address these uncertainties, but none have yet demonstrated the precision and stability necessary for Δ_{47} measurements.

Spectroscopic techniques, however, show great promise for measuring stable isotopologue abundances in natural samples because they are non-destructive, sensitive to both mass and molecular symmetry, and field-deployable. These characteristics are particularly desirable for studying the stable isotope distribution in atmospheric gases, and how they evolve over time. The author has had some experience with these techniques so the following discussion represents a synthesis of his experience. While most examples relate to CO_2, the general considerations presented here should be applicable to spectroscopic stable isotope measurements of other species. More general and thorough reviews of the literature have been published (e.g., *Kerstel* [2004]; *Kerstel and Gianfrani* [2008]), so the references herein are exemplary rather than comprehensive.

Three main instrumental requirements for highly precise optical measurements of rare and/or 'clumped' isotopologues near natural isotopic abundance are apparent: absolute sensitivity, dynamic range, and long-term signal stability. A more subtle problem is the selection of spectral region; the spectral absorption scales not only with analyte concentration, but also the optical pathlength and the size of the transition dipole (i.e., the absorption line strength, S, for the transition). In addition, spectral overlap between isotopologues and also from contaminants will lead to systematic errors. The type of spectroscopic technique, then, will depend on the analyte identity and spectral region. For instance, *Tuzson et al.*

[2008] used the strong CO_2 lines ($S \sim 10^{-18}$ cm molecule^{-1}) near 2300 cm^{-1} and a multi-pass direct absorption cell [*Herriott et al.*, 1964] to measure δ^{13}C and δ^{18}O with better than 0.1‰ precision (100-s averaging). The authors utilized that region because the transitions for $^{12}C^{16}O_2$, $^{13}C^{16}O_2$, and $^{16}O^{12}C^{18}O$ were of nearly equal strengths. *Bergamaschi et al.* [1994] made similar line choices for δ^{13}C and δD measurements in CH_4. *McManus et al.* [2002] surmounted the dynamic range problem for their CO_2 isotopologue measurements by designing an optical cell with differential absorption pathlengths for each isotopologue, allowing CO_2 lines differing in intensity by several orders of magnitude to be measured precisely. In both cases, long-term drifts (e.g., temperature, laser power, frequency jitter etc.) were accounted for by simultaneous measurement of a reference gas.

Other important variables to consider are sample temperature stability and spectral line function. *Bergamaschi et al.* [1994] reported an approximate sensitivity of the measured δ-value and temperature (T) in per-mil units:

$$\frac{\Delta\delta}{\Delta T} \approx \frac{\Delta E}{kT^2} \times 1000 \tag{2.10}$$

where k is Boltzmann's constant and ΔE is the difference in lower-state energies of the corresponding transitions. It is derived from the Taylor series expansion of a normal (Gaussian) distribution [*Schupp*, 1992]. Empirically, this translates to $\pm$ 5‰ K^{-1} for bulk stable isotope measurements of H_2O and CO_2 [*Kerstel and Gianfrani*, 2008], so a temperature stability between the reference gas and the sample of 50 mK would yield temperature-induced errors of 0.1‰. *Kerstel and Gianfrani* [2008] also make the argument that measurement of peak intensities is sufficient so long as the lineshape functions are the same between the sample and standard transitions.

'Clumped' isotope measurements present a new set of concerns due to the more stringent technical demands, e.g., measuring a signal 4.5 $\times$ 10^{-5} with 0.005‰ precision for Δ_{47}-based carbonate thermometry [*Huntington et al.*, 2009]. At present, high-precision IRMS measurements of Δ_{47} involve multiple comparisons between the sample CO_2 gas, bulk stable isotope working standards, and 'clumped' stable isotope standards (CO_2 with a stochastic distribution of isotopologues). Any spectroscopic technique will require similar calibrations

because the instrument response, in general, will not be sufficiently linear over such a large range in concentration. For instance, the required linear dynamic range for rovibrational transitions of $^{12}C^{16}O_2$ and $^{16}O^{13}C^{18}O$ with identical v and J (absolute sensitivity concerns notwithstanding) is $\geq 10^9$. Photoacoustic methods are capable of this dynamic range, in principle, but previous attempts to make high-precision isotopic measurements have been limited by fluctuations in pump laser power [*Samura et al.*, 2002]. On the other hand, if a convenient spectral window is found such that line strengths of the dominant and minor isotopologues are similar, the temperature sensitivity will be large (e.g., due to large differences in the lower-state energies).

From a practical perspective, the line strength of the minor isotopologue will dictate the choice of method; for instance, the strongest $^{16}O^{13}C^{18}O$ transition in the mid-IR has a line intensity $S \sim 10^{-23}$ cm molecule^{-1}, which is out of range for all but the most sensitive spectroscopic techniques. Of the high-sensitivity optical techniques, cavity ringdown spectroscopy (CRDS; *O'Keefe and Deacon* [1988]) with frequency-axis stabilization and single-mode operation (FS-CRDS; [*Hodges et al.*, 2004]) shows the most promise, in this author's opinion. A key feature in FS-CRDS is its ability to average spectra on the timescales of hours; the utility of other ultrasensitive methods, such as the shot-noise-limited NICE-OHMS technique (noise-immune, cavity-enhanced optical heterodyne molecular spectroscopy) [*Ye et al.*, 1998], have been ultimately limited by technical pitfalls and long-term drifts [*Foltynowicz et al.*, 2008]. In contrast, FS-CRDS can be averaged continuously for nearly 10 hours to achieve a signal-to-noise ratio (SNR) of 18,000 (i.e., 0.6‰ precision) on a single line of intensity $S = 1 \times 10^{-24}$ cm molecule^{-1} at 0.5 Torr [*Long et al.*, 2009]. Higher SNRs may be possible with the implementation of single-mode optical feedback [*Motto-Ros et al.*, 2008], optoelectronic laser-locking [*Drever et al.*, 1983], or in combination with rapid (kHz) sample-background ringdown comparison [*Ye and Hall*, 2000]; increasing sample concentration will also improve the SNR, but the dynamic range of the instrument will place an upper limit on the maximum line strength. The choice of lineshape theory used to obtain the integrated intensity might also be important [*Lisak et al.*, 2006, 2009], as the integrated intensity is a more robust measurement of isotopic abundance than

peak height, which increases nonlinearly with gas pressure.

At present, IRMS is the only practical method for measuring 'clumped' isotopologue abundances in in CO_2 with precisions better than 0.1‰. Spectroscopic measurements for CO_2 will be best in the mid-IR region, where the rovibrational transitions are strongest ($S_{^{16}O^{13}C^{18}O} \sim 10^{-23}$ cm molecule^{-1}); single-mode quantum-cascade lasers with $\geq$ 5 mW power are becoming widely available in that region. Another possibility for CO_2 is the 2-μm region, where the strongest $^{16}O^{13}C^{18}O$ line strength is $S_{^{16}O^{13}C^{18}O} \sim 3 \times 10^{-26}$ cm molecule^{-1} (4826.05 cm^{-1}); analysis time will be increased accordingly. The NICE-OHMS method is capable of reducing analysis times significantly, in principle, because it has demonstrated a shot-noise-limited sensitivity for strong laser sources (e.g., SNR = 7700 in 1s for $S = 1 \times 10^{-23}$ cm molecule^{-1} using a 5 mW Nd:YAG) [*Ye and Lynn*, 2003; *Ye et al.*, 1998]. However, technical challenges such as long-term temperature and frequency stability must be addressed.

While examining the possibility for measuring 'clumped' CO_2 isotopologues spectroscopically is useful for illustrating the general principles involved, this approach will ultimately be the most useful for other species of atmospheric and geochemical interest. For instance, isotopic abundances in SO_2 are canonically difficult to measure due to its polarity [*Gao and Thiemens*, 1991, 1993]; high-precision IRMS systems rely on a viscous-flow injection into the ionization region, and high-polarity gases such as SO_2 often display a pronounced 'memory' effect that limits measurement precision and reproducibility [*Ono et al.*, 2006]. SO_2 lines in the mid-IR ($\sim$2500 cm^{-1}) are of comparable strength to those of CO_2 in the 2-μm region (see above), so 'clumped' isotopologue measurements of SO_2 may be possible, with long averaging times, in the near future. These measurements have the potential to establish a link between the ancient atmosphere and the geologic record. For instance, *Lyons* [2009] has proposed that the unique sulfur and oxygen isotope composition of Archaean Fig-tree barites [*Bao et al.*, 2007] may reflect gas-phase SO_2–H_2O isotope exchange reactions; 'clumped' isotope analysis would place additional constraints on the origins of these and other barites, which contain information about the sulfur and oxygen cycles, atmospheric composition, and climate of the ancient past.

2.C Low-temperature cell for $^{13}C/^{12}C$ KIE experiments

For the low-temperature $^{13}C/^{12}C$ KIE experiments, the quartz reaction chamber (filled with N_2O, CO_2, and He) was placed inside a cooling assembly within a conflat vacuum chamber. The vacuum chamber was first pumped down to ∼20 – 50 mTorr, and then liquid N_2 coolant (ΔH_{vap} = 1.33 kcal mol^{-1}) was added through a feedthrough at the top of the chamber. The liquid N_2 cooled a series of metal ("conduction" and "transfer") blocks, which, in turn, cooled the quartz reaction cell along its entire length. Temperature was monitored using a standard type-K thermocouple; active temperature control was possible, though it was not necessary to achieve temperatures near 230 ± 1 K when the liquid N_2 was poured into the feedthrough.

The cooling assembly was designed to fit inside a spare ∼27 × 27 × 21 cm ($l \times w \times h$, interior dimensions) conflat chamber with a 9.5-cm ID (see Figures 2.11, 2.12, and 2.13). Experimental and spatial constraints dictated the design parameters, and the resulting assembly had little flexibility. Use of 193-nm laser radiation to photolyze N_2O meant that quartz (UV-grade fused silica) windows were the most affordable and robust window material; MgF_2 windows can provide ∼10% greater transmission at 193 nm, but quartz was chosen because it was cheaper and could be bonded with a quartz tube to make a monolithic, leak-tight reaction chamber without need for adhesives. During an experiment, the reaction chamber was inserted directly into the oxygen-free, high conductivity (OFHC) copper tube (2.14). This tube was fastened to the "conduction block" (Figure 2.15), which was itself attached to the OFHC copper "heat-transfer block" by a countersunk screw on the rounded underside of the conduction block. A second heat-transfer block (Figure 2.17) was sandwiched between the heat-transfer block and the connection to the liquid N_2 feedthrough (Figure 2.18); this block had a relatively small surface area and was machined out of brass (120 W m^{-1} K^{-1} vs. 401 W m^{-1} K^{-1} for copper at 300 K) to retard heat transfer from the liquid N_2 to the reaction cell. The second heat-transfer block also had a hole drilled through the center so a heating resistor could be inserted, if necessary, to control the temperature in future experiments.

All components were mated with a thin layer of Apiezon "N" grease; this material was

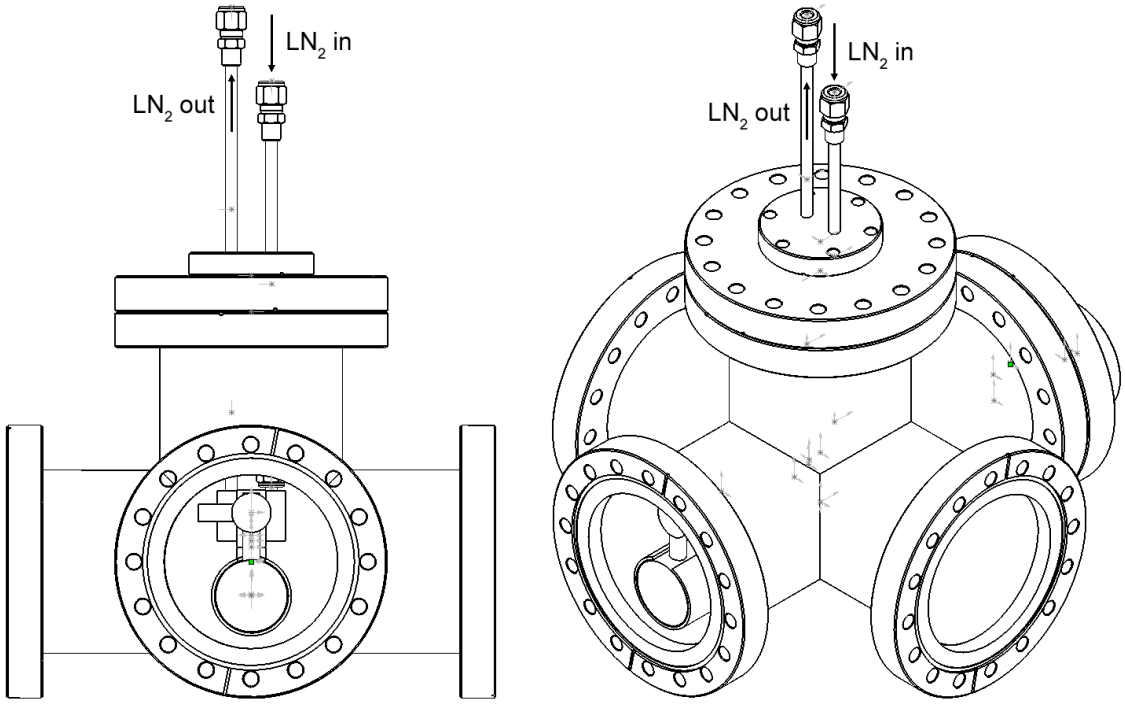

Figure 2.11: **Schematic of conflat chamber used for low-temperature $^{13}C/^{12}C$ KIE experiments.**

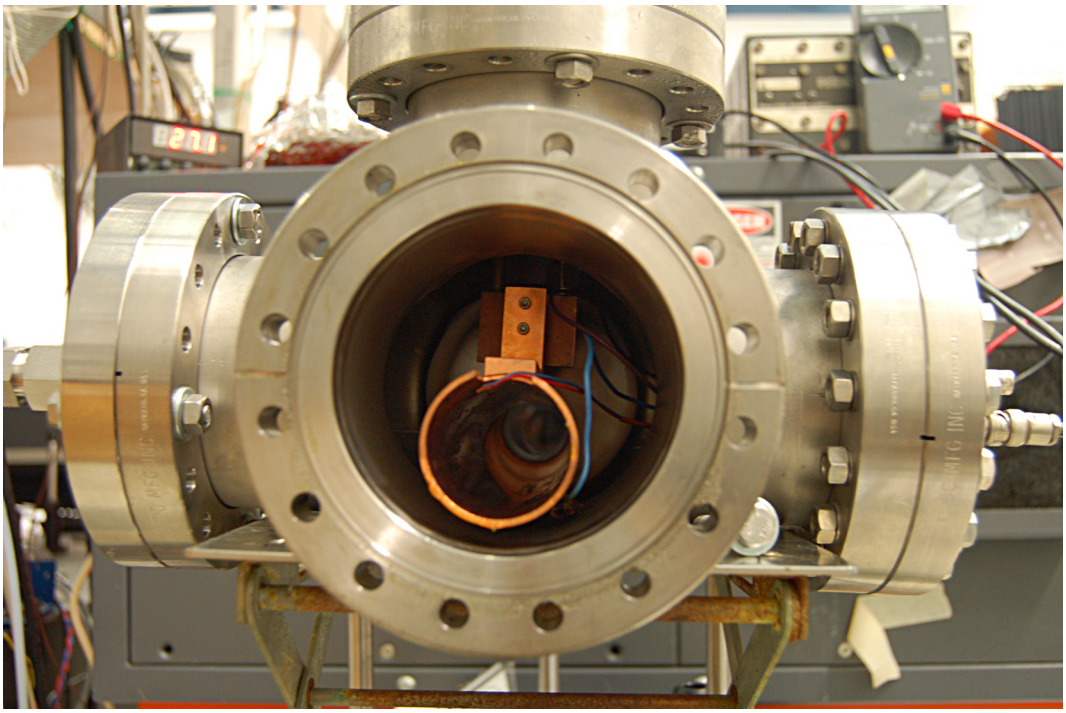

Figure 2.12: **Photograph of conflat chamber used for low-temperature $^{13}C/^{12}C$ KIE experiments.**

chosen over other compounds because of its ability to perform at low temperatures (down to liquid He), low coefficient of thermal expansion ($\leq 10^{-4}$ K^{-1}) and minimal thermal creep. However, it has a very low thermal conductivity (0.1 – 0.2 W m^{-1} K^{-1}), which slowed the cooling process. Typically, the assembly took 40 – 60 min to cool from 300 K to 229 K. While higher-efficiency thermal compounds would have accelerated cooling of the reaction chamber, Apiezon "N" was sufficient to achieve stable temperatures above 200 K.

Small modifications were made to the cooling assembly for planned $O(^1D)$ + CH_4 and OH + CH_4 KIE experiments (see Figure 2.19). Because the target temperatures for those experiments are 140 K $\leq$ T $\leq$ 200 K, the two "heat-transfer" blocks were combined into a single OFHC copper heat-transfer block with a larger contact area with the existing "conduction block" (see Figures 2.20 and 2.21). The primary cooling block was smoothed (the shallow channel removed) to mate well with the new conduction block. Last, metal-to-metal mating surfaces were cleaned and the Apiezon "N" grease replaced with a thermal paste containing silver particles (thermal conductivity $\sim$ 9 W m^{-1} K^{-1}). With this new assembly and the pressurized delivery of liquid N_2 from a free-standing dewar into the feedthrough, the quartz reaction cell was cooled to temperatures of $\sim$140 K within 10 min. Temperature control electronics are currently being designed.

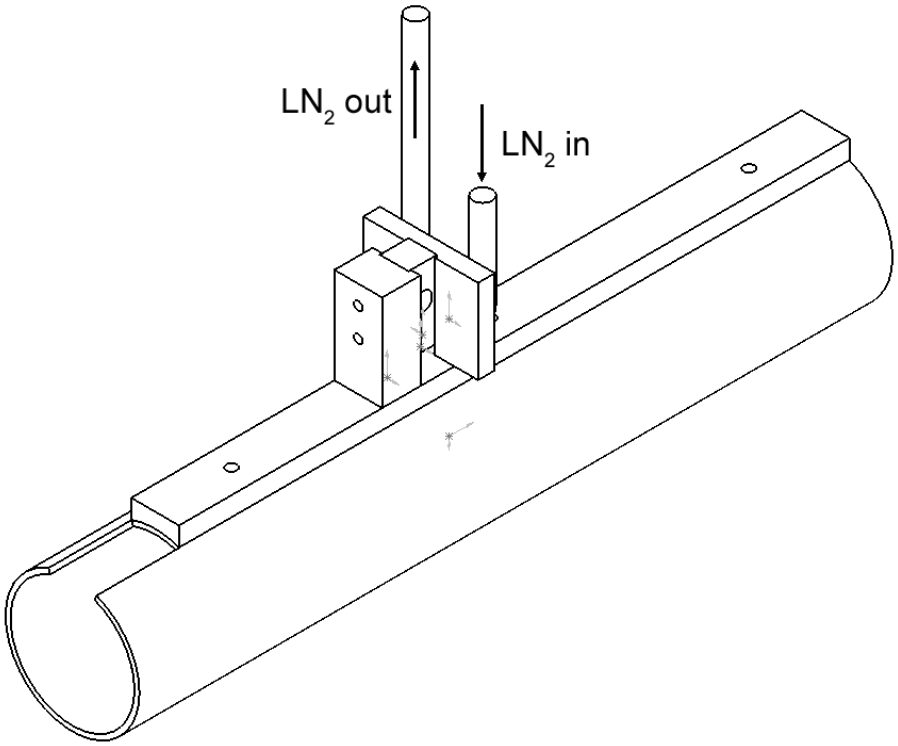

Figure 2.13: **Cold cell assembly.**

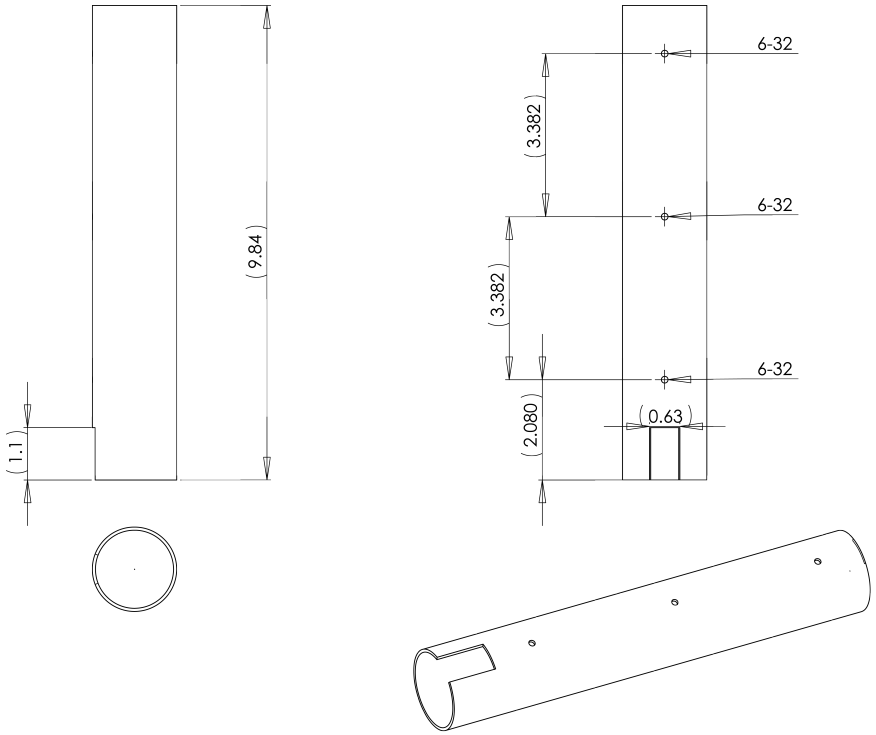

Figure 2.14: **Machining diagram for the OFHC copper tube.**

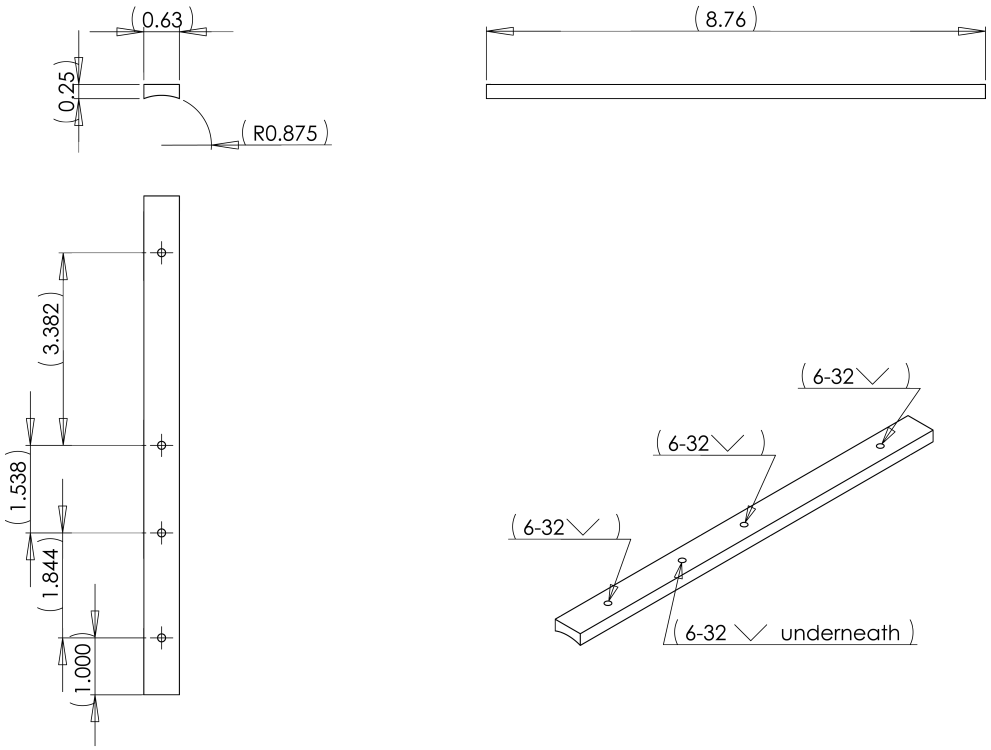

Figure 2.15: **Machining diagram for the OFHC copper conduction block.**

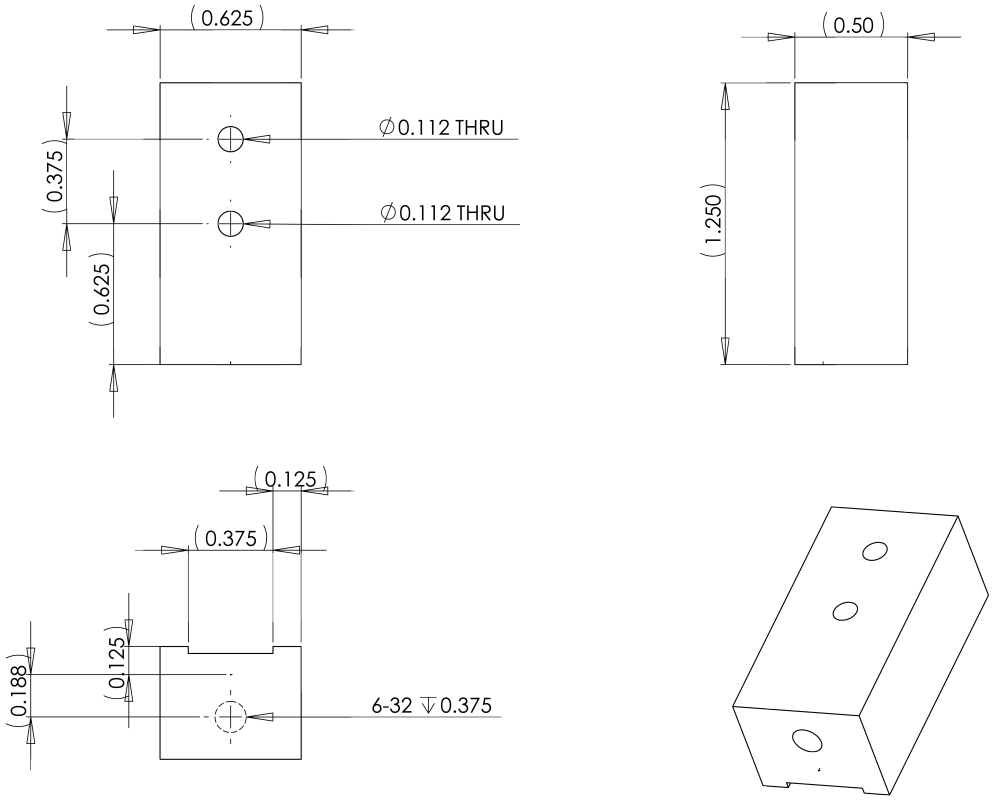

Figure 2.16: **Machining diagram for the OFHC copper heat transfer block.**

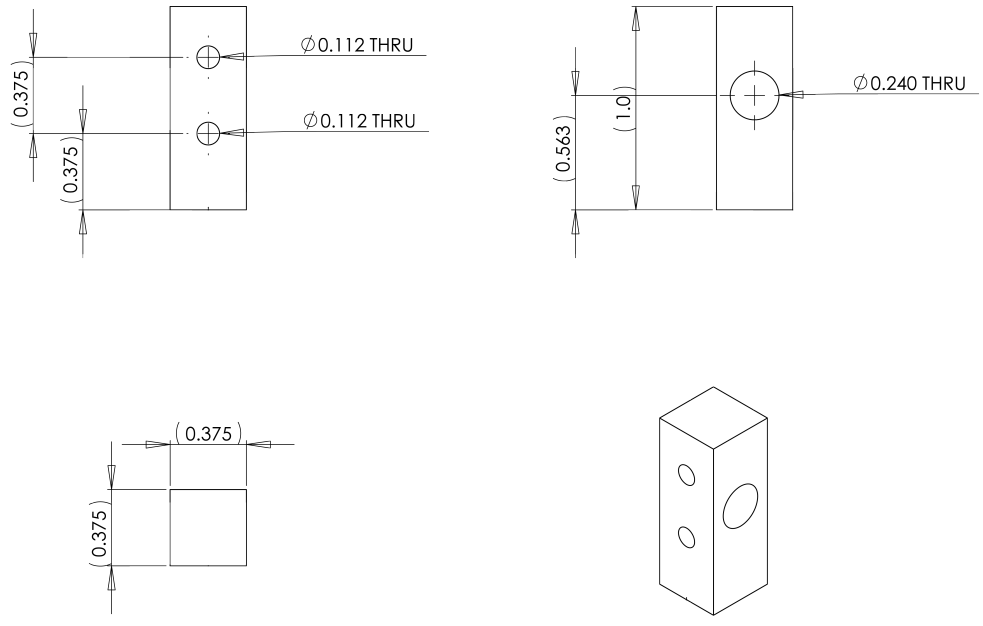

Figure 2.17: **Machining diagram for the brass heat transfer block.**

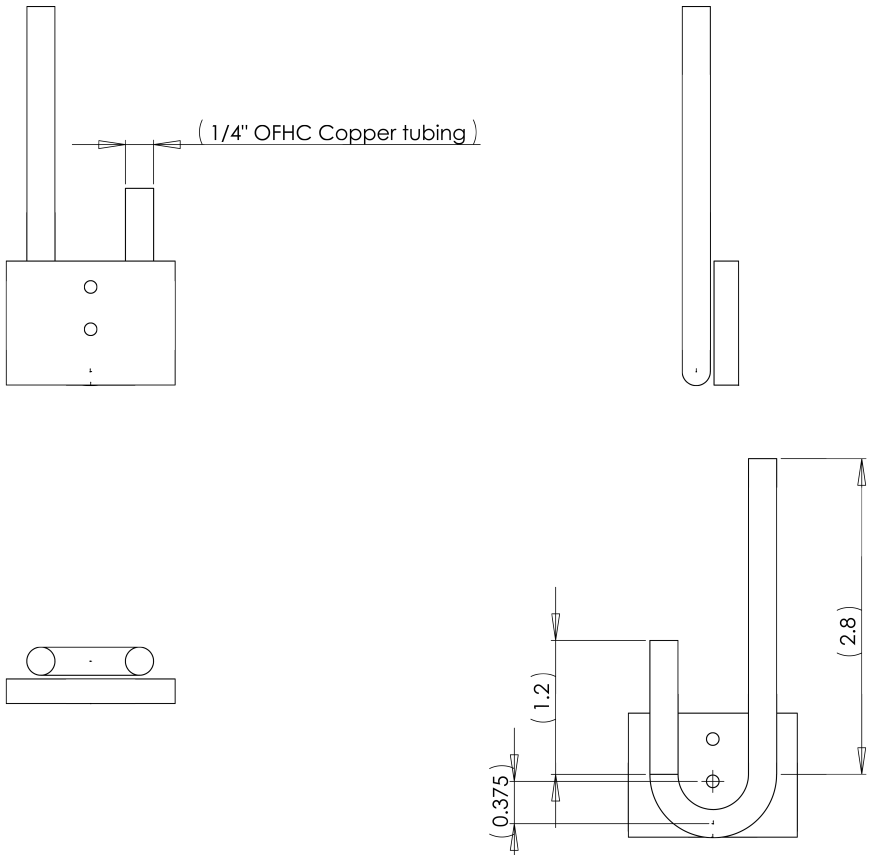

Figure 2.18: **Machining diagram for the OFHC copper connection to the liquid N_2 feedthrough.**

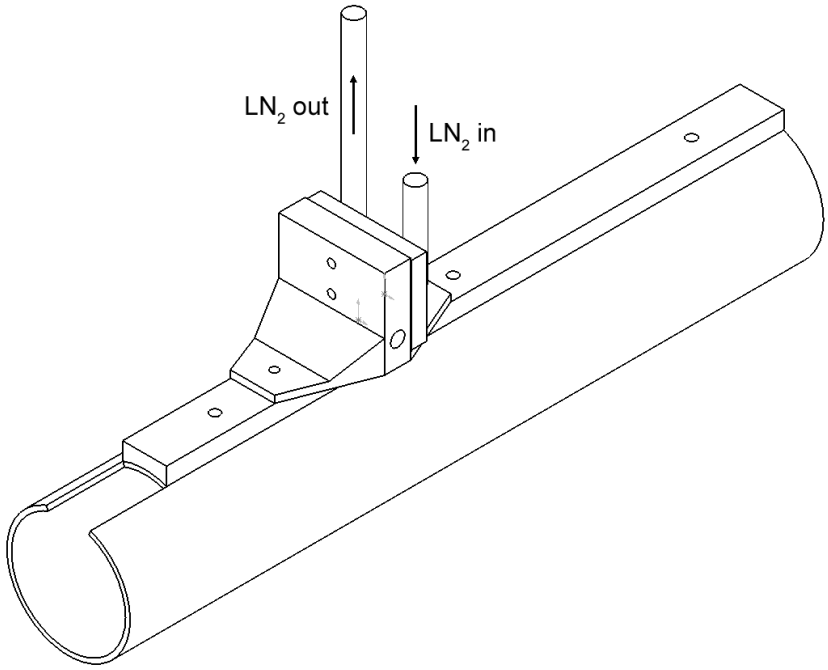

Figure 2.19: **Cold cell assembly for O(^1D), OH + CH_4 KIE experiments.**

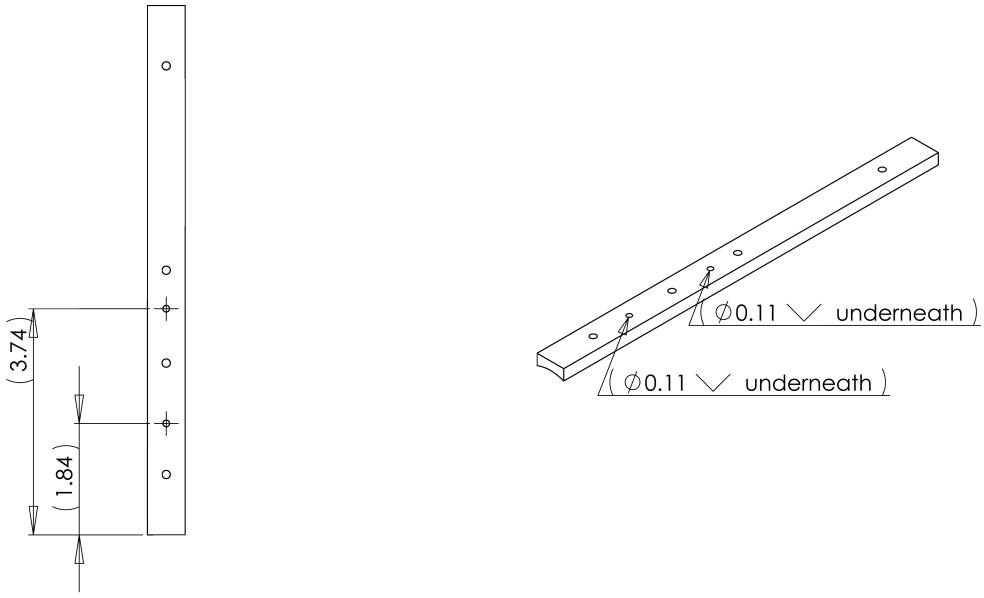

Figure 2.20: **Machining diagram illustrating the modifications made to the conduction block for O(^1D), OH + CH_4 KIE experiments.**

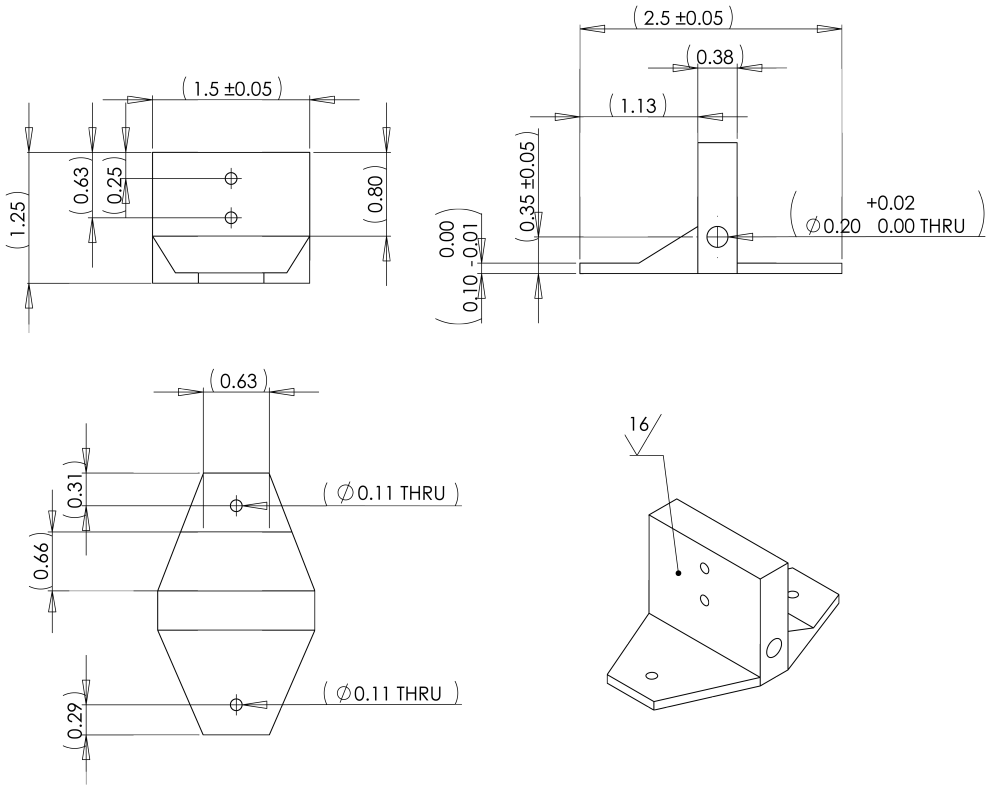

Figure 2.21: **Machining diagram for the OFHC copper heat transfer block designed for O(^1D), OH + CH_4 KIE experiments.**

2.D MATLAB code for hard-sphere collision model

2.D.1 montecarlo.m

```
% Program for calculating 18O(1D)+CO2 collision energy in experiments

clear x y z j v1i v2i r;
points=50000;
% number of points per collision
T=300;
% temperature in K
m1=18;
% mass of O(1D)
m2=4;
% mass of buffer gas (He: 4, N2: 28)
mCO2=44;
ET2lab=18.2; %8.6 for O3 photolysis at 248 nm
% Etrans (kcal/mol) in the Lab frame
Equil=(3/2)*8.314472/4.184/1000*T;
% Equipartition energy
vOpeak=sqrt((ET2lab*1000*4.184*2)/(m1/1000));
% O(1D) atom velocity
vMreduced=vOpeak/sqrt((Equil*1000*4.184*2)/(m2/1000));
% buffer gas velocity in units of O(1D) velocity
%vMreducedCO2=vOpeak/sqrt((Equil*1000*4.18*2)/(mCO2/1000));
ncolltot=200;
% Number of collisions
zz=zeros(points,ncolltot);
% distribution of final O(1D) velocities
zzz=zeros(points,1);
% distribution of initial O(1D) velocities
CO2=zeros(points,ncolltot);
% distribution of collision energies with CO2
dist=zeros(points,ncolltot);
% distribution of buffer gas velocities
PM=97; %1-380e-6 for 'stratospheric'
% pressure of buffer gas in Torr
PCO2=3; %380e-6 for 'stratospheric'
% pressure of CO2 in Torr
Pcoll=PCO2/(PCO2+PM);
% ratio of CO2 to buffer gas (reaction probability per collision)

for l=1:ncolltot
    nPcoll(l)= Pcoll*(1-Pcoll)^(l-1);
    % multiplied by (1-(3.1e-11/1e-10))^(l-1) for 'stratospheric'
    % fraction of O(1D) that reacts at each collision
end
digits(10);
nPcoll=vpa(nPcoll);
for j=1:points
    ncoll=1;
    v1i=randn*exp(-1.5)+vMreduced;
% pick a random v for O(1D) from a gaussian distribution about vMreduced
    zzz(j)=v1i;
% record the velocity in a matrix
```

```
    theta1i=rand*3.14159265359;
% pick a random azimuthal angle between 0 and pi for O(1D)
    phi1i=rand*2*3.14159265359;
% pick a random azimuthal angle between 0 and 2pi for O(1D)
    v2i=randn;%metropolis([v2i,5]);
    theta2i=rand*3.14159265359;
% pick a random azimuthal angle between 0 and pi for M
    phi2i=rand*2*3.14159265359;
% pick a random azimuthal angle between 0 and 2pi for M
    while (phi1i < phi2i)
        phi2i=rand*2*3.14159265359;
% prevents imaginary results in scatter function
    end
    impact=rand^2;
% pick a random (b/bmax) with probability proportional to itself
    omega=rand*3.14159265359;
% pick a random azimuthal angle for b between 0 and pi
    while (ncoll ≤ ncolltot)
% calculate O(1D) trajectory for n collisions
        vrel=sqrt((v1i*sqrt(mCO2/m2))^2+v2i^2-2*v1i*v2i*(sin(theta1i)*
            sin(theta2i)*cos(phi1i-phi2i)+cos(theta1i)*cos(theta2i)));
        % calculating initial relative velocity
        CO2(j,ncoll)=((1/2)*((mCO2*m1/(mCO2+m1))/1000)*(vrel*
            sqrt((Equil*1000*4.184*2)/(mCO2/1000)))^2)/(4.184*1000);
            % calculate initial collision energy w/CO2
        v1f=scatter(m1, m2, v1i, theta1i, phi1i, v2i, theta2i,
            phi2i, impact, omega);
        % calculate final velocity after one more collision
        zz(j,ncoll)=real(v1f);
% record the final velocity
        dist(j,ncoll)=v2i;
% record in initial velocity of M
        v1i=real(v1f);
% reset initial velocity as the final velocity after a collision
        theta1i=rand*3.14159265359;
% pick a new azimuthal angle for O(1D)
        phi1i=rand*2*3.14159265359;
% pick a new polar angle for O(1D)
        v2i=randn;
% pick a new velocity for M
        theta2i=rand*3.14159265359;
% pick a new azimuthal angle for M
        phi2i=rand*2*3.14159265359;
% pick a new polar angle for M
        while (phi1i < phi2i)
% prevents imaginary results in scatter program
            phi2i=rand*2*3.14159265359;
        end
        impact=rand^2;
% pick a new impact parameter (b/bmax)
        omega=rand*3.14159265359;
% pick a new scattering angle
        ncoll=ncoll+1;
% rinse, repeat
    end
end
bins=250;
% number of bins
```

```
upperlimit=25;
% range, 0 — upperlimit
binsvector=zeros(1,upperlimit);
% generating empty histogram bin vector to improve performance
for c=1:bins
    binsvector(1,c)=(upperlimit/bins)*c;
% generating histogram bins
end
[Ppercollision,bin]=histc(CO2,binsvector);
% generating binned histogram matrix of CO2, Ppercollision
for k=1:ncolltot
% each column is reactive probability distribution at that collision
    Ppercollision(:,k)=Ppercollision(:,k)*double(nPcoll(k));
% each column is weighted by the fraction of remaining O(1D) atoms
end
Ecollavg=sum(CO2)/points;
% average collision energy at each collision number
dlmwrite('v1i.csv',zzz);
% write matrix of initial O(1D) velocities to file, v1i.csv
dlmwrite('v1f.csv',zz);
% write matrix of final O(1D) velocities to file, v1f.csv
dlmwrite('Ecollpercollision.csv',CO2);
% write matrix of per—collision collision energies to file
dlmwrite('Ppercollision.csv',Ppercollision);
% write binned histogram matrix of CO2 to file, Ppercollision.csv
```

2.D.2 scatter.m

```
% Function solving the two—particle scattering problem

function v1f=scatter(m1, m2, v1i, theta1i, phi1i, v2i, theta2i, phi2i,
    impact, omega)

vrel=sqrt(v1i^2+v2i^2—2*v1i*v2i*(sin(theta1i)*sin(theta2i)*
    cos(phi1i—phi2i)+cos(theta1i)*cos(theta2i)));
    % relative veocity calculation
v1c=(m2*vrel)/(m1+m2);
% v1 (O(1D)) in the COM frame
v2c=(m1*vrel)/(m1+m2);
% v2 (M) in the COM frame
vcm=sqrt(m1^2*v1i^2+m2^2*v2i^2+2*m1*m2*v1i*v2i*(sin(theta1i)*
    sin(theta2i)*cos(phi1i—phi2i)+cos(theta1i)*cos(theta2i)))/(m1+m2);
    % velocity of the COM
thetacm=acos((m1*v1i*cos(theta1i)+m2*v2i*cos(theta2i))/((m1+m2)*vcm));
% azimuthal angle in the COM frame
phicm=acos((m1*v1i*sin(theta1i)*cos(phi1i)+m2*v2i*sin(theta2i)*
    cos(phi2i))/((m1+m2)*vcm*sin(thetacm)));
    % polar angle in the COM frame
alpha=acos((v1i^2—(vcm^2+v1c^2))/(2*vcm*v1c));
% azimuthal scattering angle in the COM frame
deflect=2*acos(impact);
% polar scattering angle in the COM frame
l=v1c*(cos(deflect)*cos(alpha)—sin(deflect)*sin(alpha)*cos(omega));
v1f=sqrt((vcm+l)^2+v1c^2—l^2);
```